K⁻p

UCRL-10779

University of California

Ernest O. Lawrence Radiation Laboratory

K^-—PROTON INTERACTIONS NEAR 760 MeV/c

Berkeley, California

UCRL-10779
UC-34 Physics
TID-4500 (19 Ed.)

UNIVERSITY OF CALIFORNIA

Lawrence Radiation Laboratory
Berkeley, California

Contract No. W-7405-eng-48

K^--PROTON INTERACTIONS NEAR 760 MeV/c

Pierre L. Bastien

(Ph. D. Thesis)

February 1963

Printed in USA. Price $1.75. Available from the
Office of Technical Services
U. S. Department of Commerce
Washington 25, D.C.

$\bar{K}$ - PROTON INTERACTIONS NEAR 760 MeV/c

Contents

K^--PROTON INTERACTIONS NEAR 760 MeV/c

Pierre L. Bastien

Lawrence Radiation Laboratory
University of California
Berkeley, California

February 1963

ABSTRACT

The interactions of K^- mesons with hydrogen, at beam momenta of 620, 760, and 850 MeV/c, have been studied in the Lawrence Radiation Laboratory's 15-inch hydrogen bubble chamber.

The cross sections for all the reactions allowed at these momenta have been measured, together with the angular distributions for the two-body final states. The energy dependence of these cross sections shows that, at 760 MeV/c, they are affected by a recently discovered resonant state, $Y_1^*(1660)$. On the basis of an analysis of the cross sections, a spin assignment of 1/2 for $Y_1^*(1660)$ is ruled out. A spin assignment of 3/2 seems to be more consistent with our data than higher spin values because of the absence of large $\cos^3\theta$ terms in the angular distributions at 760 MeV/c.

I. INTRODUCTION

Two years ago very little was known about the K^- meson-proton (K^--p) system. Interactions at rest, and up to a laboratory-system momentum of 400 MeV/c, had been studied by Ross, Humphrey, and Nordin, and interactions at 1.15 BeV/c by Graziano and Wojcicki.[1,2,3] A great unexplored range otherwise existed between these two momenta, and it appeared of considerable interest to set up an experiment that would cover some of the region.

The detector would be a hydrogen bubble chamber, ideally suited for a systematic study of K^--p interactions, since all kinematically overdetermined reactions can be accurately measured in such an instrument. Consequently, during the summer of 1960 the Lawrence Radiation Laboratory's 15-inch hydrogen bubble chamber was irradiated with K^- mesons at a large series of momentum settings. We have analyzed all the interactions at three of these momenta: 620, 760, and 850 MeV/c.

Owing to the exploratory nature of the experiment and the lack of previous theoretical knowledge of the K^--p system at these energies, it was difficult at first to orient the research along very specific lines. A posteriori, however, it appeared that no less than five of the recently discovered resonant states were produced in the region: $Y_0^*(1405)$, $Y_0^*(1520)$, $Y_1^*(1385)$, $Y_1^*(1660)$ and the η meson.[4]

We decided to center the discussion in this paper around $Y_1^*(1660)$ for two reasons:

(a) The $Y_1^*(1660)$ is a resonance that affects the whole energy region under consideration. It is a strangeness-1, I-spin 1 state originally discovered in high-energy π^--p and K^--p interactions.[5,6] In these high-energy experiments the $Y_1^*(1660)$ was produced together with an additional pion (see Fig. 31). In our experiment no additional pion is produced; the $Y_1^*(1660)$ is formed by the initial K^--p system and then decays into all the two- and three-body final states that can be produced at our energies.[7] Furthermore, since the central value of the resonance (1660 MeV) and its full width (40 MeV) correspond to K^- laboratory-system momenta of 715 ± 90 MeV/c, the whole energy region is affected.

(b) A statement can be made about its previously undetermined spin. Assuming that the resonance is adequately described by a Breit-Wigner amplitude--as has been done very successfully by Ferro-Luzzi et al. in the analysis of a similar state, $Y_0^*(1520)$--the spin can, in principle, be obtained rather easily by examining the energy dependence of the cross sections and angular distributions.[8] A definitive answer to the spin question is not presented because we have too few data points in the resonance region. However, spin 1/2 is ruled out by the behavior of the cross sections. The angular distributions indicate that spin 3/2 appears to be more consistent with our data than higher spin values.

This paper is divided into three sections. Section II is devoted to the experimental procedure; in particular, the data-analysis system is described in detail. In Section III, the cross sections and angular distributions are presented, together with a brief discussion of the biases and ambiguities encountered in the experiment. Finally, in Section IV is examined what can be said about the production and the quantum numbers of $Y_1^*(1660)$ on the basis of the observations. Also the gross features of the K^--p system at these energies are discussed.

II. EXPERIMENTAL PROCEDURE

Before physical quantities can be extracted from a bubble chamber experiment the following preliminary operations must be completed:

(a) Designing and building the beam of particles with which the chamber will be irradiated;

(b) Scanning the film obtained for all interactions or events, which are then measured on a digitizing microscope;

(c) Writing a number of computer programs whose function is to reconstruct the events in space, fit them to certain kinematical hypotheses, and extract physical quantities of interest from them.

This section explores these aspects of the experiment.

A. Beam

The beam was designed to operate under a great variety of conditions, most of which are irrelevant for the purposes of this paper.[9] Only the numbers of interest to us are listed here.

A layout of the beam is shown in Fig. 1. The beam emerged from the Bevatron tank with a momentum of 800 MeV/c. The first quadrupole Q_1 was used to obtain parallelism in the first spectrometer. This glass-cathode spectrometer was capable of holding an electric field of 90 kV/cm with a plate separation of 5 cm.[10] Q_2 brought the beam back to a stigmatic focus at the first slit S_1: this permitted the use of a wedge absorber to reduce the momentum spread from approx 1% to 0.5%. At S_1 the pion intensity was 3×10^5 pions per 10^{11} protons with the first spectrometer set to transmit pions, and 1.5×10^4 pions per 10^{11} protons with the spectrometer set to transmit K^- mesons. The K^- intensity at S_1 was 150 per 10^{11} protons. The beam was then deflected 38 deg by the magnet M_1; this freed it from a considerable fraction of the off-momentum pions. The second stage was very similar to the first. At the second slit S_2 the K^-/π^- ratio was 6/1, and 10 K^- mesons per 10^{11} protons entered the chamber. At the center of the chamber the beam had a momentum of 762 ± 7 MeV/c. A setting at 620 ± 15 MeV/c was obtained by degrading the beam with a slab of

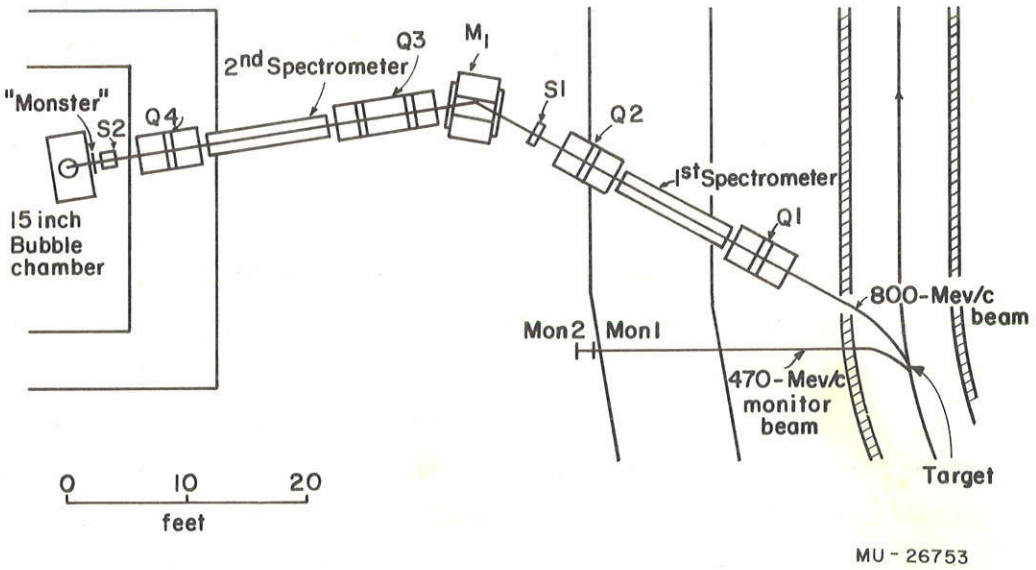

Fig. 1. Layout of the 800-MeV/c K^- beam at the Berkeley Bevatron (October 1960 - January 1961).

copper. An 850 ± 10 MeV/c beam at the center of the chamber was also made available by changing the position of the target in the Bevatron tank. This last beam had a K^-/π^- ratio of 4/1 at the second slit.

B. Scanning and Measuring

For each expansion of the bubble chamber, four stereo pictures were taken. The film was scanned once by a group of trained technicians. The scanner was not asked to make a specific identification of the reaction, but merely to record the topological appearance of the event. The task of identifying the events was left to the fitting programs, at a later stage in the processing.

The various topologies found in the experiment, together with the corresponding reactions, are listed in Table I. All these reactions are analyzed in this paper, except those belonging to (2-prong + V) events, which are the object of a separate study by Berge.[11] However, some of this author's results are important for our analysis and they have been quoted whenever necessary. Also omitted from the list are 0-prong and 1-prong events, which are not considered in this study.

Scanning efficiencies were obtained by rescanning approximately 30% of the film. The efficiencies deduced from this second scan are listed in Table II.

At the time of the scan the only interactions accepted for further processing were those that occurred in a central region of the chamber. This region is called the fiducial volume. Its projection on the scanning table, as seen by a camera, is shown on Fig. 2. It appears as the octagon delimited by the fiducial marks scratched on the top window of the chamber. Only in that region is the illumination uniform and all the tracks of an event long enough to provide adequate momentum measurements. An event was defined as being in the fiducial volume if all its vertices were inside the octagon, which meant that an escape correction had to be calculated for multivertex events. Also, to guard against possible biases on the part of the scanner in borderline

Table I. Topologies and the corresponding reactions

Topology	Reaction
2-Prong	$K^- p$, $\bar{K}^0 p\pi^-$, $K^-\pi^+ n$, $K^-\pi^0 p$, $\Lambda\pi^+\pi^-$, $\Sigma^0\pi^+\pi^-$, $\Lambda\pi^+\pi^-\pi^0$
2-Prong ±[a]	$\Sigma^-\pi^+$, $\Sigma^+\pi^-$, $\Sigma^-\pi^+\pi^0$, $\Sigma^+\pi^-\pi^0$
0-Prong + V	$\bar{K}^0 n$, $\bar{K}^0 n\,\pi^0$ $\Lambda\pi^0$, $\Sigma^0\pi^0$, $\Lambda\pi^0\pi^0$, $\Sigma^0\pi^0\pi^0$, $\Lambda\eta$[b]
2-Prong + V	$\Lambda\pi^+\pi^-$, $\Lambda\pi^+\pi^-\pi^0$, $\Lambda\eta$, $\Sigma^0\pi^+\pi^-$, $\bar{K}^0 p\pi^0$
3-Prong	τ

a. (2-Prong +) means a 2-Prong in which the positive prong subsequently decays.

b. Not energetically possible at 620 MeV/c.

Table II. Scanning efficiencies

Topology	Efficiency (%)
2-Prong	94.5
2-Prong + V	95.0
2-Prong +	96.7
2-Prong -	95.5
0-Prong + V	89.0
3-Prong	97.0

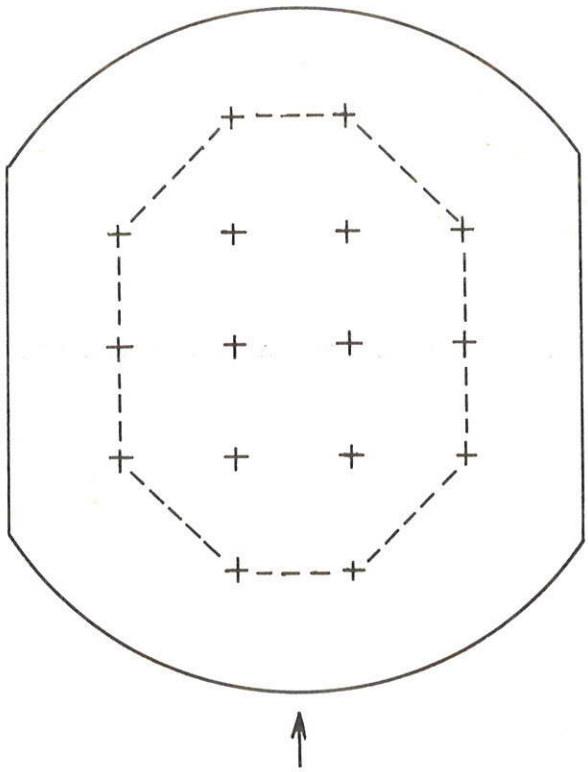

MU-30612

Fig. 2. Top view of a bubble chamber picture as seen on a scanning projector. The "+" signs represent the fiducial marks scratched on the top window of the chamber. The dashed line delimits the fiducial volume.

cases, and to ensure uniformity in cross-section calculations, a program later rejected any event for which at least one of the vertices was outside a region slightly smaller than this fiducial volume.

All events in the fiducial volume were then sketched to help the measurer. The two stereo views from which every track of an event should be measured were indicated on the sketch. The criteria for selecting the views were (a) that the stereo angle should be the most favorable one, and (b) whenever possible, that there should be no turbulence and a minimum number of crossing background tracks.

The coordinates of two to ten points along each track in the stereo pair of photographs were then measured on a digitizing microscope called Franckenstein.[12] These coordinates were punched on IBM cards, together with identifying information and the coordinates of two of the fiducial marks.

All (0-prong + V), (2-prong +), (2-prong -), and 3-prong events in the fiducial volume were measured. On the other hand, only 30% of the 2-prongs were measured: 80% of the events in this topology are K^--p elastic scatterings for which the cross section is high, and measuring a third of them gave adequate statistics on that reaction. The total number of events measured, at all three momenta in these five topologies, was 8650.

C. Data-Analysis System

Once an event had been measured it entered into a complex system of programs. Most of these programs belong to the Alvarez Group Programming System, and some others were written specifically for this experiment. In the description that follows, all the programs belonging to the Alvarez Group Programming System have been referenced to the original programmers.

The system was designed to be automatic, in the sense that no manual bookkeeping should be necessary.

There were two sorts of data input to this system:

(a) Franckenstein cards: the IBM cards obtained on each event from the measuring projector,

(b) Master List cards: a master list established by punching one

card for each event recorded on the scanning table. This card contained roll and frame number, beam momentum, topology, and possibly the scanner's comments on the event, mainly on the ionization of the tracks.

Figure 3 shows how the programs of the data-analysis system were interconnected. The Franckenstein cards were input to PACKAGE, a combination of two subprograms:

(a) PANG, which reconstructed the events in space, calculated curvatures and assigned errors.[13] The problems of error assignments in the 15 inch chamber, and their consequences, have been discussed in detail by Ross and Humphrey.[1]

(b) KICK, which attempted a fit to all the overdetermined reactions of a given topology.[14] It put out a measure of the goodness of fit to each of these reactions in the form of a χ^2. At the same time it gave the fitted laboratory-system quantities for all the reactions, together with the error matrices.

Also, in KICK, the important step of beam averaging took place before the fitting. The beam momenta (p_{beam}) were known from beam studies to an accuracy of 1%. The beam momenta calculated by the PANG program from curvature measurements (p_{pang}) were accurate only to 5%. All the tracks were therefore beam-averaged; namely, the momentum of the beam track used in the fitting was given by

$$p = \frac{p_{pang}\,\delta p_{beam}^2 + p_{beam}\,\delta p_{pang}^2}{\delta p_{pang}^2 + \delta p_{beam}^2}\,, \qquad \text{(II-1)}$$

instead of simply p_{pang}. The appropriate error on that quantity was also calculated in the beam-averaging routine.

The KICK output was of little value by itself, so that a program was needed to calculate the physical quantities of interest on an event, such as center-of-mass angles, missing masses, etc. This was done by EXAMIN, which wrote these numbers out, together with identifying information, at the rate of one record per event, on what was called a Data Summary Tape (DST).[15]

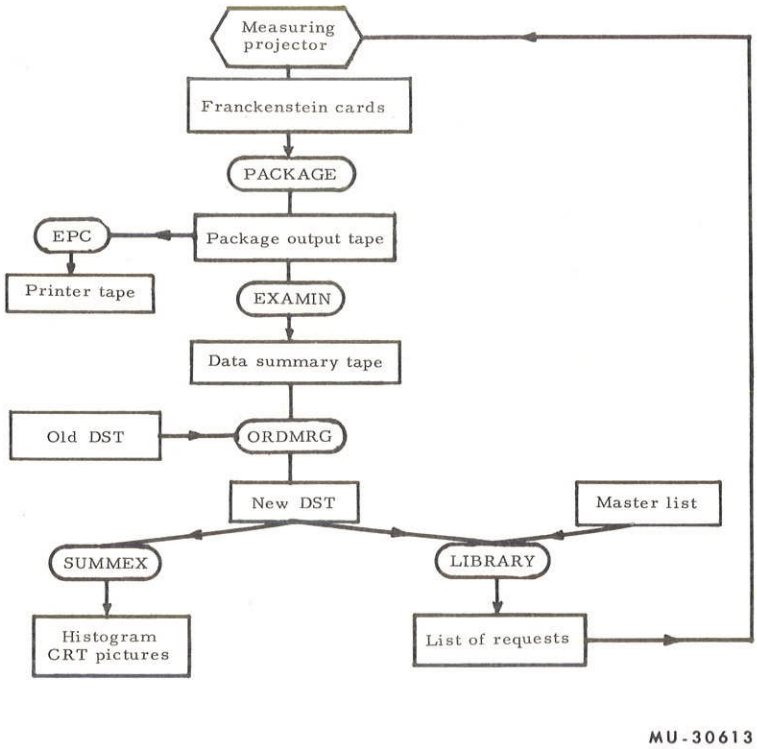

Fig. 3. Flow diagram of the data-analysis system.

A program called ORDMRG ordered this DST by roll and frame, updated the previously existing DST by merging it with this new one, and eliminated possible duplicate events.

The DST served as input to two programs:

(a) SUMX, which made a histogram or an ideogram of any quantity appearing on the DST records; furthermore, very general selective criteria could be applied on other words of the record, to determine whether the event would be counted.[16,17]

(b) LIBRARY, which compared the DST and the Master List and put out two lists: one of events that appeared on both the DST and the Master List, and another of events that appeared on the Master List only. An accurate status of the experiment was therefore immediately available every time the DST had been updated.

Finally, to help determine why certain events did not fit a single hypothesis, one last program was necessary. This program, EPC, listed all the laboratory-system quantities on events that failed.

Event failures were of three types:

(a) Approximately 20% of the events processed were rejected by the PANG part of the PACKAGE program. The subprogram PANG caught most of the gross mistakes of the measurers, such as unacceptable stereo angles, missing tracks, etc. These events were remeasured until they passed PANG and went to the KICK part of PACKAGE.

(b) Approximately 10% of the events entering KICK were rejected. These rejects were in general due to a small kink in one of the tracks which had passed unnoticed during the first scan, or because the event was generally difficult to measure. These events, after having been examined on the scanning table, were remeasured once or at most twice, according to special instructions given to the measurer. By that time, 98% of the events recorded on the scanning table were accounted for.

(c) The remaining 2% were events for which it was hopeless to attempt a fit because of turbulence, missing views, too many crossing tracks, or for some other reason. These events were abandoned and the appropriate corrections were made when calculating cross sections.

III. CROSS SECTIONS AND ANGULAR DISTRIBUTIONS

A discussion of biases and ambiguities in the interpretation of the events for the various topologies is given in this section. All the results on cross sections, angular distributions, and polarizations are collected in the second part of the section.

A. Biases and Ambiguities

The reactions are divided according to topologies, since ambiguities can occur only between reactions of a given topology. The ambiguities that must be dealt with are of two kinds. First, the final states of a given topology are overdetermined. These events can therefore be fitted, but in a given event several of these fits have given good χ^2. Secondly, the reactions of the topology are underdetermined, and to separate them one has to resort to missing-mass spectra. These, in general, are such that the range of missing masses expected of one final state overlaps the spectrum expected of another final state. We specify in what sense the word "ambiguity" is being understood when it is used.

The discussion of biases and ambiguities given here is not exhaustive, since these problems are by now well understood in bubble chamber physics at the energies we used. Instead, the main difficulties are summarized and an explanation of how they were solved is given.

1. 2-prong events. The possible reactions are listed in Table I. All are overdetermined except $\Lambda\pi^+\pi^-\pi^0$, which can be ignored, since only five events of that type are expected to be present in the whole sample, on the basis of the study of (2-prong + V) events (see Table III for the number of events in the various reactions). Two- and three-body final states can be separated unambiguously at our energies, and two-body events, namely K^--p elastic scatterings, are considered first.

The first problem encountered in K^--p scatterings is a 10% contamination due to π^--p scatterings, whose existence has already been mentioned in the section on the beam. These two reactions overlap kinematically when the meson scatters forward. The number of π^--p scatterings in that region can be easily estimated, since we can find the angular distributions for our backward π^--p scatterings and know the overall differential cross section for π^--p scattering at these energies from other experiments.[18] Our backward π^--p differential cross section was therefore extrapolated in the forward direction and a subtraction was made.

When the K^- scatters in the forward direction, the recoil proton is short and scanning efficiencies drop sharply. A cutoff of $\cos\theta = 0.9$ was applied, where θ is the center-of-mass angle of the scattered K^-. At 620 MeV/c this corresponds to a length of 2 cm for the proton recoil. As seen on the scanning table, the recoil is only 1.2 cm long on the average. But such a length, together with the fact that the film was scanned in two stereo views, is sufficient to ensure high efficiencies. This was checked by plotting a histogram of the angle between the normal to the plane of scattering and the vertical direction. Such a distribution should be flat, and has been found to be so within two standard deviations, for this cutoff, at all three momenta.

The possible three-body final states are listed in Table I. Except for $K^-\pi^+n$ and $K^-p\pi^0$, which can appear only as 2-prongs, all the others can also appear as (2-prong + V) events. When an event fitted several of the three-body hypotheses it was sometimes possible to identify the positive prong as being a proton or a pion, on the basis of ionization. When this information was not available, or was still inconclusive, a decision was made on the basis of the best χ^2.

2. <u>(2-prong +) and (2-prong -) events</u>. The possible reactions in these topologies are

$$K^- + p \rightarrow \Sigma^- + \pi^+ , \qquad \text{(III-1)}$$

$$K^- + p \rightarrow \Sigma^+ + \pi^- , \qquad \text{(III-2)}$$

and

$$K^- + p \rightarrow \Sigma^- + \pi^+ + \pi^0 , \qquad \text{(III-3)}$$

$$K^- + p \rightarrow \Sigma^+ + \pi^- + \pi^0 . \qquad \text{(III-4)}$$

KICK can easily differentiate a $\Sigma\pi$ from a $\Sigma\pi\pi$ final state. A small source of contamination in (2-prong -) events is due to K^-p elastic scatterings in which the K^- subsequently decays. This hypothesis was tried in KICK, and such events are easily separated from events involving a Σ.

One has to contend with two types of biases:

(a) The Σ's that go backward have small laboratory-system momenta and are sometimes quite short: in some instances they even have zero length, then appear as 2-prongs. Although this has not been mentioned so far, every 2-prong was fitted to the hypothesis of a zero-length Σ. Not all those events could be found, however, since only 30% of the 2-prongs were measured. Therefore all the 2-prong Σ's were discarded, and a cutoff of 2.5 mm was further applied to all visible Σ's to ensure high scanning efficiencies. All Σ's shorter than 2.5 mm were discarded, and a weight calculated for all the others. The probability that a Σ would be shorter than 2.5 mm is given by

$$P_1 = \int_0^{t_1} \frac{1}{\tau_\Sigma} \exp[-t/\tau_\Sigma]\, dt, \qquad \text{(III-5)}$$

where t_1 is the time it takes the Σ in its rest frame to go from the interaction point up to a length of 2.5 mm.

As stated, all the vertices of an event had to be inside the fiducial volume for that event to be measured. The probability that a Σ would escape is given by

$$P_2 = \int_{t_2}^{\infty} \frac{1}{\tau_\Sigma} \exp[-t/\tau_\Sigma]\, dt, \qquad \text{(III-6)}$$

where t_2 is the time taken by the Σ in its rest frame to reach the boundary of the region.

The overall weight on an event was then

$$w = 1/(1 - P_1 - P_2)\,. \qquad \text{(III-7)}$$

(b) Σ^+'s decaying via the pionic mode ($\Sigma^+ \to \pi^+ n$) are easily detected, but the efficiency for finding Σ^+'s decaying via the protonic mode

($\Sigma_0^+ \to p\pi^0$) is very small in certain regions. Indeed, at our energies, the laboratory-system momenta for Σ_0^+'s going forward in the center-of-mass system are quite large, and the angle between the Σ_0^+ and its decay proton is usually small and not easily detected. To find the size of this bias, we have plotted in Fig. 4 the distribution of the angles between the Σ_0^+'s and their decay protons as they appeared on the scanning table for a given sample of Σ^+'s. On the same graph, the angle between the Σ_4^+'s and their decay neutrons have been plotted as they would have appeared if the neutrons were visible. The two distributions should be identical but we find instead that there is a severe bias for small-angle Σ_0^+ decays. For this reason, the Σ_0^+ events were not used in our cross-section and angular distribution calculations.

3. <u>(0-prong + V) events</u>. This topology, by far the most difficult to handle, was crucial for our experiment. The final states are again listed in Table I. They fall into two obvious and easily separated categories; those involving a Λ^0 hyperon and those involving a $\overline{K}^0$. Separating the reactions within the first of these categories is difficult and we take it up in detail in a subsequent paragraph.

The separation of $\overline{K}^0$ and Λ offers almost no difficulties, since virtually all the events for which the V fits a $\overline{K}^0$ and a Λ are such that the fitted $\overline{K}^0$ momentum exceeds the beam momentum by more than three standard deviations. In other words, we would have

$$\frac{P_{\overline{K}^0}^{\text{fitted}} - P_{\text{beam}}}{\delta p_{\overline{K}^0}^{\text{fitted}}} > 3 \qquad \text{(III-8)}$$

for most of those ambiguous events, and this is physically impossible.

The few events that still remain ambiguous after this test can be separated on the basis of the ionization of the positive prong of the decay of the V.

As for Σ events the same cutoff of 2.5 mm was applied to all V's, and escape corrections were calculated. The overall weight on each event is the same as that given by Eq. (III-7).

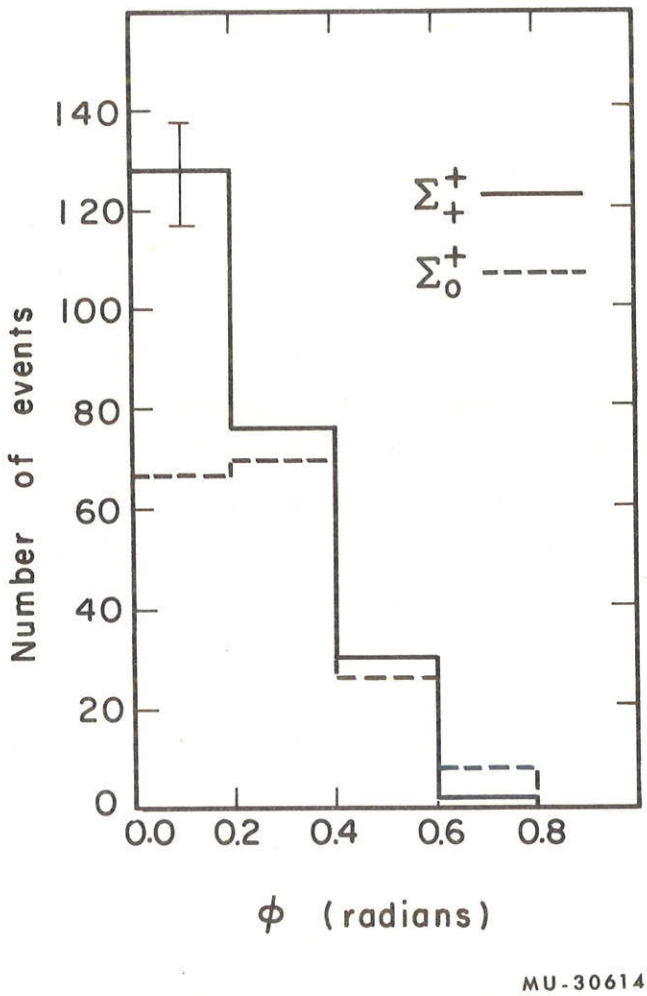

Fig. 4. Number of Σ_+^+ (solid line) and Σ_0^+ (dashed line) as a function of the angle between the Σ^+ and its decay nucleon for a sample of Σ^+ events.

Separation of the $\bar{K}^0 n$ and $\bar{K}^0 n\pi^0$ events is most easily done by plotting μ^2, the square of the invariant mass coming from the $(\bar{K}^0, K^-)$ system. The expected μ^2 spectrum for $\bar{K}^0 n$ events is a delta function at $(0.939)^2$ BeV^2, whereas the $\bar{K}^0 n\pi^0$ spectrum begins at 1.15 BeV^2. Since the errors on μ^2 are of the order of 0.035 BeV^2, the separation is clean. Let us now consider the problem of separating the following final states:

$$K^- + p \rightarrow \Lambda + \pi^0 \qquad \text{(III-9)}$$

$$K^- + p \rightarrow \Sigma^0 + \pi^0, \quad \Sigma^0 \rightarrow \Lambda + \gamma, \qquad \text{(III-10)}$$

$$K^- + p \rightarrow \Lambda + \pi^0 + \pi^0, \qquad \text{(III-11)}$$

$$K^- + p \rightarrow \Sigma^0 + \pi^0 + \pi^0, \quad \Sigma^0 \rightarrow \Lambda + \gamma, \qquad \text{(III-12)}$$

and

$$K^- + p \rightarrow \Lambda + \eta. \qquad \text{(III-13)}$$

All these reactions are, for all practical purposes, underdetermined. Here again the invariant mass squared recoiling against the (K^-, Λ) system is plotted on Figs. 5 through 7. The reason for using the mass squared instead of simply the mass is that the error on the mass squared is much more nearly Gaussian than the error on the mass.[19] The expected limits of μ^2 for the five final states under consideration are indicated on the figures. Since the theoretical shapes of the spectra are known, all that was done was to adjust their heights, and take measurement errors into account, so as to get a good overall fit. These shapes are as follows: $\Lambda\pi^0$ and $\Lambda\eta$ are delta functions; the $\Sigma^0\pi^0$ spectrum is flat because the Σ^0 has spin 1/2; the $\Lambda\pi^0\pi^0$ and $\Sigma^0\pi^0\pi^0$ spectra were assumed to follow their phase space distributions. This last is a very good approximation, since no strong pion-pion interactions have been observed in this energy range, if one excepts the η particle. We note also that the phase-space distributions for $\Lambda\pi^0\pi^0$ and $\Sigma^0\pi^0\pi^0$ overlap and are indistinguishable.

The plots on Figs. 5, 6, and 7 are ideograms. Each event is plotted as a Gaussian curve whose surface is equal to the weight calculated in Eq. (III-7), whose width is equal to the error on the missing mass squared, and those central value is equal to the observed value of μ^2. All these Gaussians are then added to form the ideogram.[20]

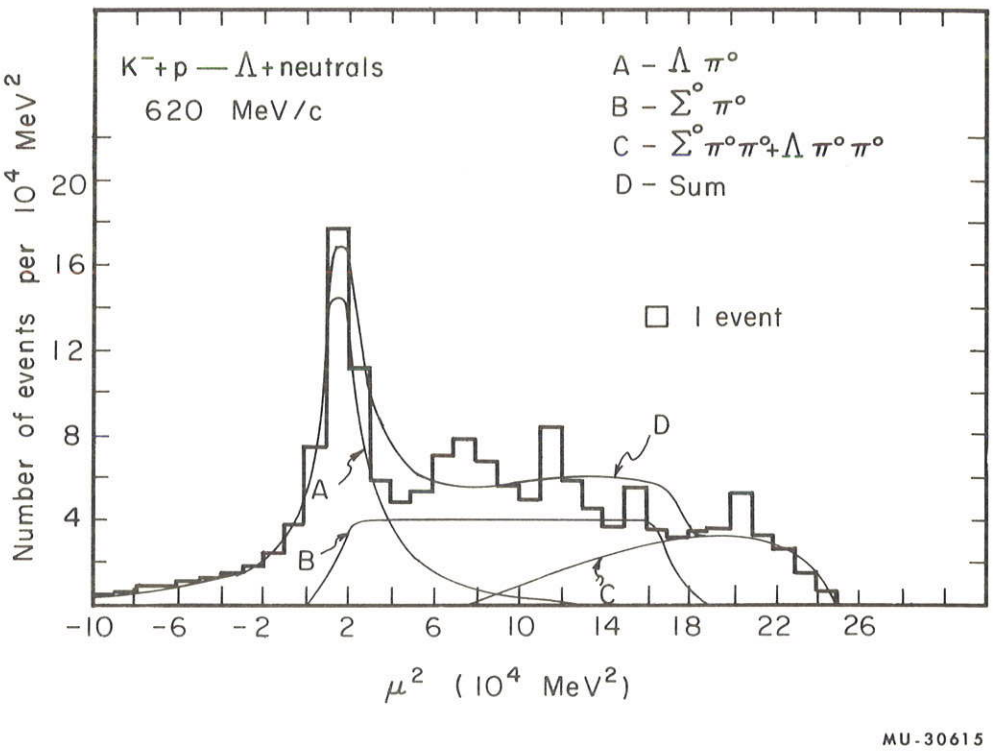

Fig. 5. Missing mass squared recoiling against the (K^-, Λ) system 620 MeV/c.

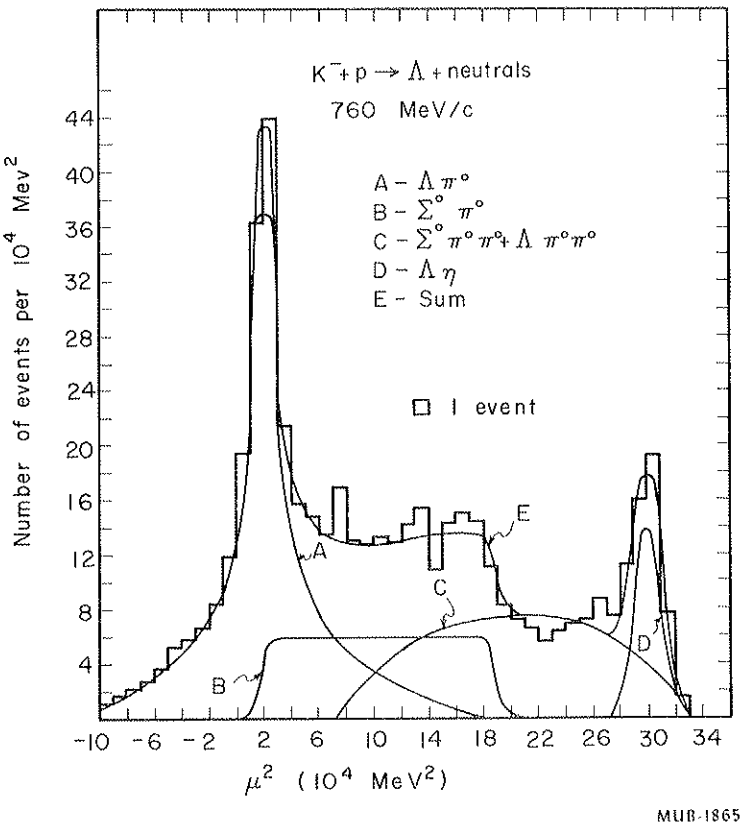

Fig. 6. Missing mass squared recoiling against the (K^-, Λ) system at 760 MeV/c.

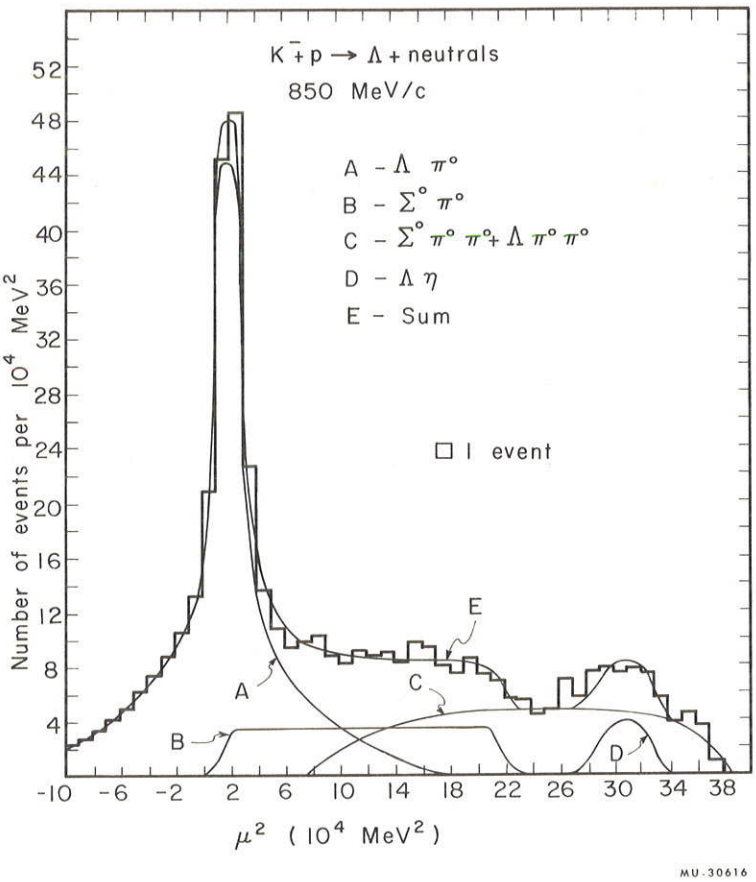

Fig. 7. Missing mass squared recoiling against the (K^-, Λ) system at 850 MeV/c.

Let us now examine the problem of obtaining the angular distribution for the $\Lambda\pi^0$ final state. An unbiased way of obtaining the distribution is to plot, at each momentum, several missing-mass spectra that correspond to different slices of the angle between the incident K^- and the Λ in the center of mass. For each of these spectra, a separation identical to the one described above can be made. The average error on μ^2 over this reduced interval is a constant that is, the error is almost independent of the position and orientation of the Λ and it is possible to represent the $\mu^2_{\pi^0}$ peak by a Gaussian curve. The number of Λ's in a slice can therefore be estimated rather easily.

The $\Sigma^0\pi^0$ angular distributions were out of reach, when the method just described was used, because the small statistics made it difficult to estimate the three-body contamination in a given bin.

B. Cross Sections and Angular Distributions

All the experimental results are gathered in this subsection. A discussion is given in the next section.

To obtain our path length, all the τ decays in the fiducial volume were counted. The disadvantage of this method is that the branching ratio for a K^- decaying into the τ mode is known only to 5.3%. This disadvantage is counterbalanced by high scanning efficiencies and the fact that the sample is absolutely uncontaminated.

The cross sections for the two-body final states were obtained by integrating the fitted angular distributions over the whole range of the c.m. angle.

The angular distributions were fitted to the series

$$k^2 \frac{d\sigma}{d\Omega} = A_0 + A_1 \cos\theta + A_2 \cos^2\theta + \cdots , \qquad \text{(III-14)}$$

where k is the wave number of the incoming state in the center of mass. Let a fit of order n be understood to mean a fit up to and including the term A_n. The input data to the program which fitted these distributions included the numbers of events observed in a given bin, together with the weights, scanning efficiencies, percentage of events abandoned, and τ-decay lifetime. The proper errors and central

values were then calculated on each bin, taking all this information into account, before the fitting took place. All numbers were then renormalized so that the coefficients would be in the units of Eq. (III-14). These numbers were then least-squares fitted, and the integral of the fitted distribution was calculated over the whole range of c.m. cosines. The error on the integral was calculated by using the complete error matrix.

The first and very important result on these angular distributions is shown in Figs. 8 through 10. We have plotted there the order of the fit vs the probability P of the fit. This last quantity, found in χ^2 tables, is

$$P = \int_{\chi_0^2}^{\infty} f(\chi^2, \nu) d\chi^2, \qquad \text{(III-15)}$$

where ν is the number of degrees of freedom and χ_0^2 the least-squares-fit χ^2 for the distribution. P is therefore a measure of the goodness of fit.

The path lengths at 620, 760, and 850 MeV/c were in the ratios of 2:5:5.

All the angular distributions are plotted in Figs. 11 through 15. The dotted curve is the order-2 fit for the 620- and 760-MeV/c distributions, and the order 3 fit for the 850-MeV/c distributions.

In Figs. 16 through 20 the values of the coefficients A_i, as a function of energy, are plotted for all the distributions. The coefficients are those obtained when fitting the distributions to order 3.

For the $\Lambda\pi^0$ final state at 850 MeV/c, we have plotted in Fig. 18 as dashed flags the values of the coefficients A_i for the order-3 and as solid flags the order-4 fits, whose probabilities P are 22% and 47% respectively. The value of A_4 in the order-4 fit is 0.16 ± 0.085, and indicates to what extent one can say that $\cos^4\theta$ is present in the distribution. This is very important for future discussions, since the value of A_2 is quite different in the two cases.

In Fig. 21 the polarizations for the reactions

$$K^- + p \rightarrow \Lambda + \pi^0; \quad \Lambda \rightarrow p + \pi^- \qquad \text{(III-16)}$$

$$K^- + p \rightarrow \Sigma_0^+ + \pi^-; \quad \Sigma_0^+ \rightarrow p + \pi^0 \qquad \text{(III-17)}$$

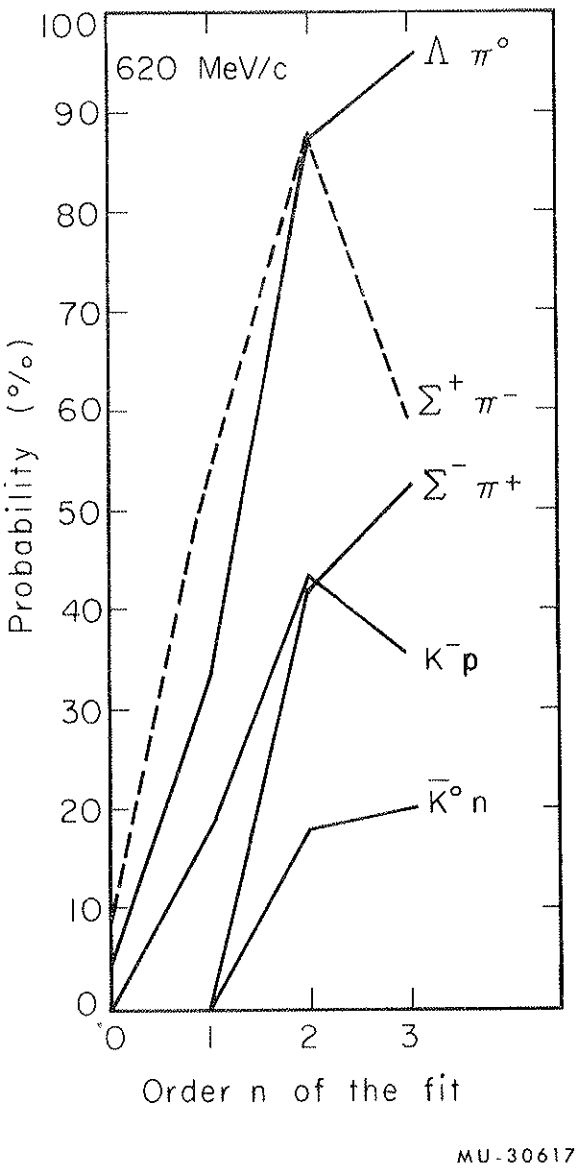

Fig. 8. Probability P as a function of the order of the fit at 620 MeV/c. The quantity P is defined in Eq. (III-15). The $\Sigma^+\pi^-$ fits are represented by the dashed line to indicate that statistics were low on that distribution.

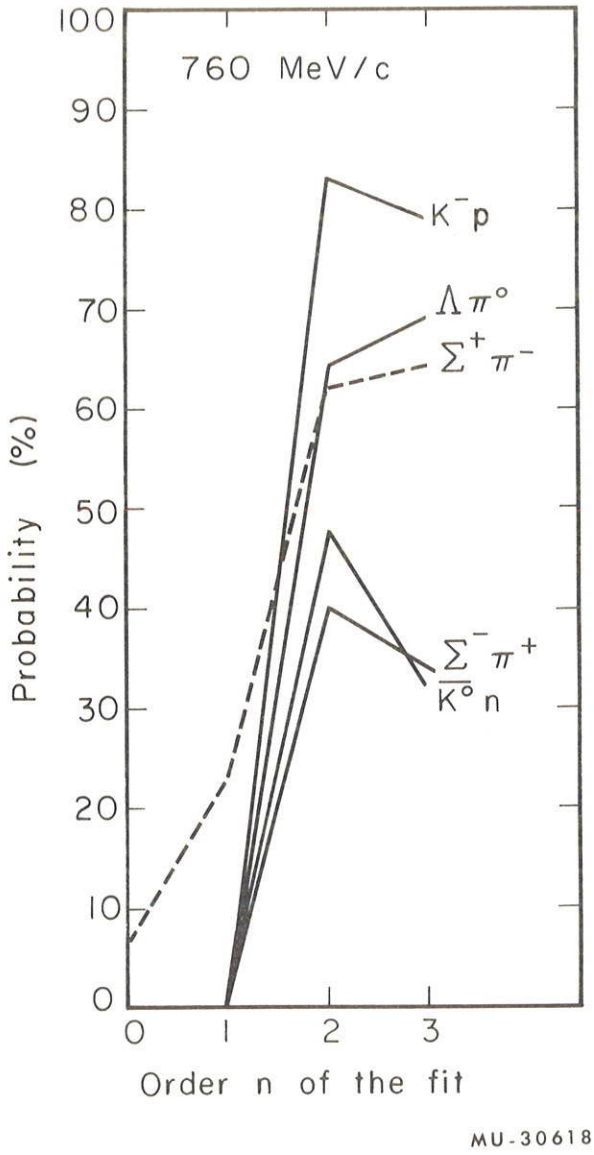

Fig. 9. Probability P as a function of the order of the fit at 760 MeV/c. The quantity P is defined in Eq. (III-15). The $\Sigma^+\pi^-$ fits are represented by the dashed line to indicate that statistics were low on that distribution.

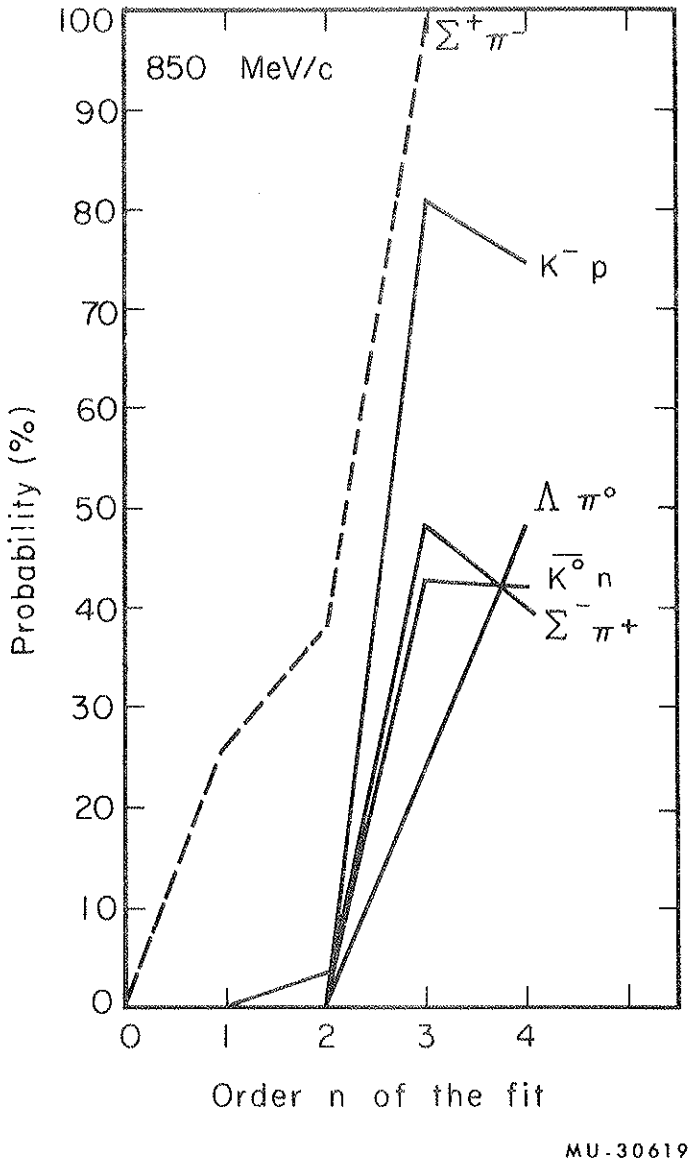

Fig. 10. Probability P as a function of the order of the fit at 850 MeV/c. The quantity P is defined in Eq. (III-15). The $\Sigma^+\pi^-$ fits are represented by the dashed line to indicate that statistics were low on that distribution. Order 3 is clearly required to fit the distributions, and $\Lambda\pi^0$ may even require order 4.

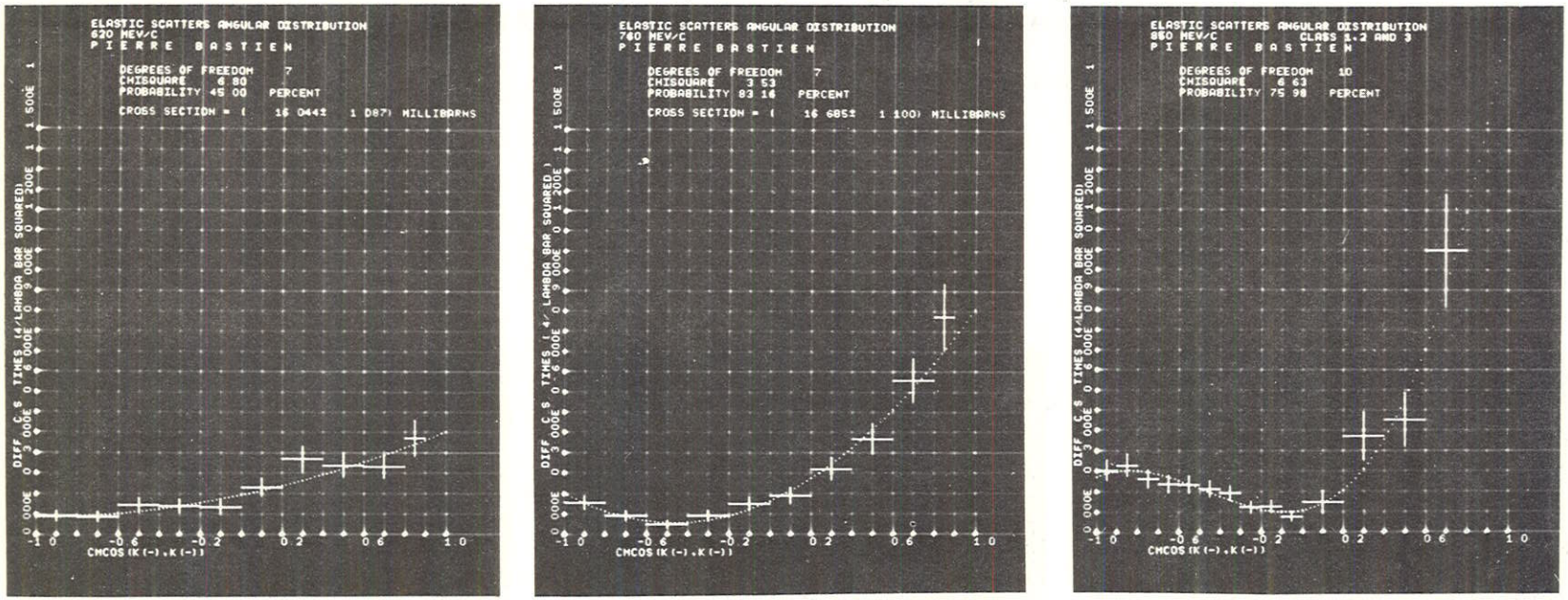

(a) (b) (c)

ZN-3794

Fig. 11. $K^- p \rightarrow K^- p$ angular distributions. The c.m. cosine is defined as $\hat{K}^-_{inc} \cdot \hat{K}^-_{scattered}$. We have (a) 620 MeV/c, (b) 760 MeV/c, and (c) 850 MeV/c.

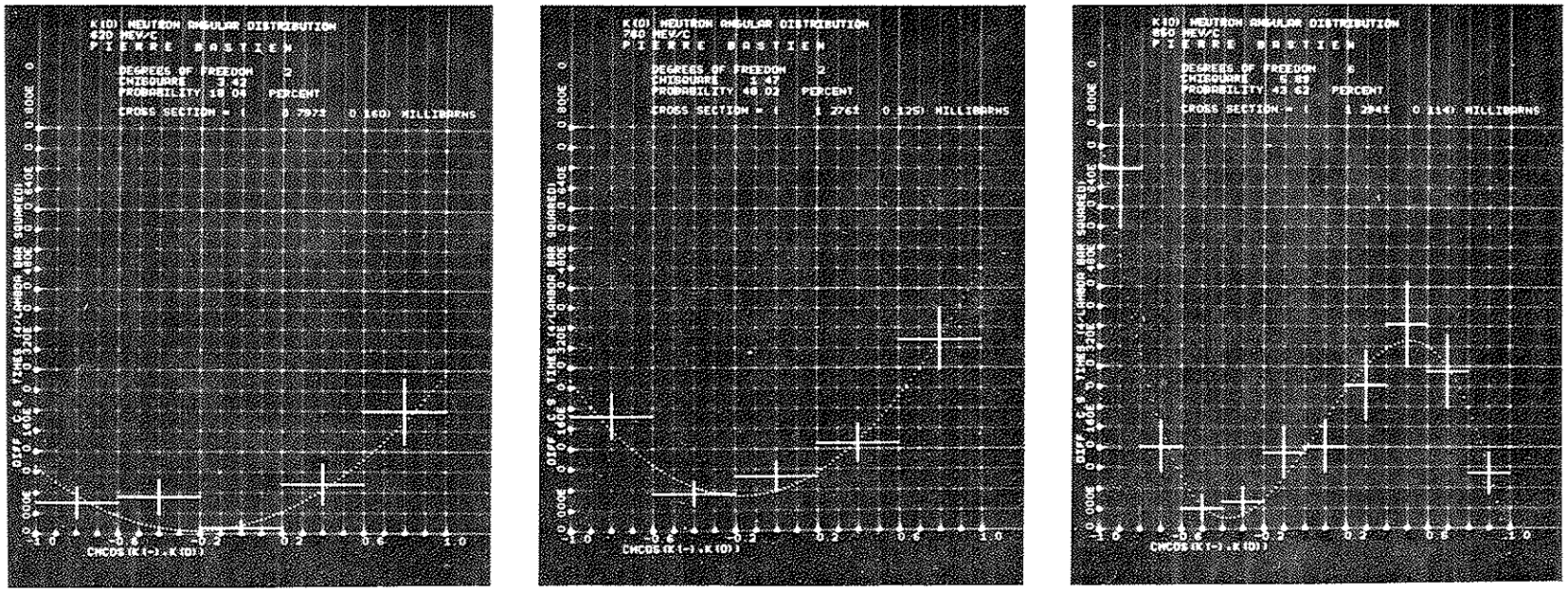

(a) (b) (c)

ZN-3795

Fig. 12. $K^- p \rightarrow \bar{K}^0 n$ angular distributions. The c.m. cosine is defined as $\hat{K}^-_{inc} \cdot \hat{K}^0$. We have (a) 620 MeV/c, (b) 760 MeV/c, and (c) 850 MeV/c.

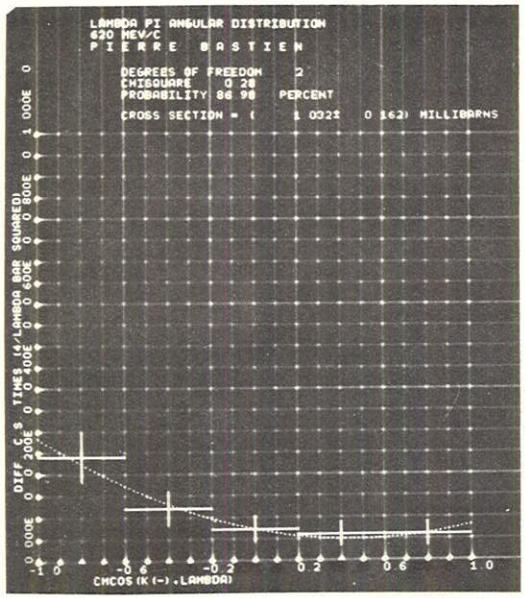

(a)

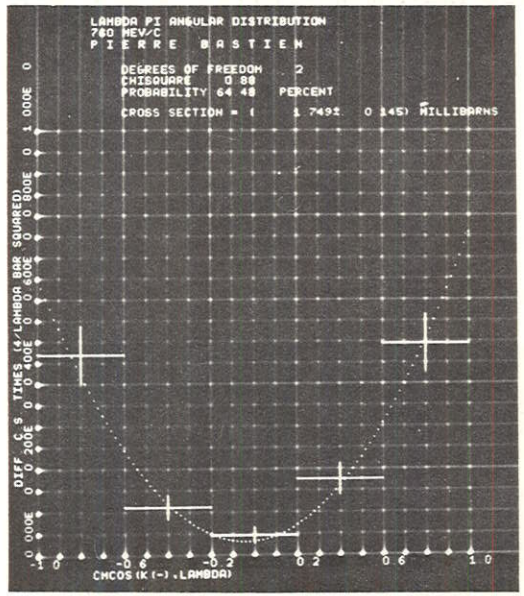

(b)

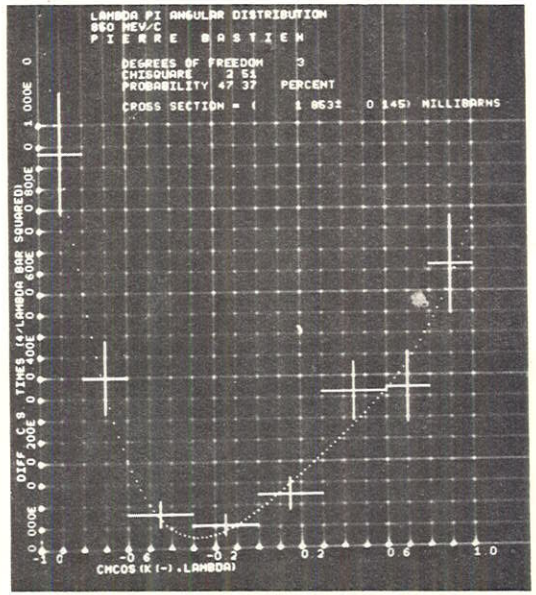

(c)

ZN-3796

Fig. 13. $K^- p \rightarrow \Lambda \pi^0$ angular distributions. The c.m. cosine is defined as $\hat{K}^-_{inc} \cdot \hat{\Lambda}$. We have (a) 620 MeV/c, (b) 760 MeV/c, and (c) 850 MeV/c.

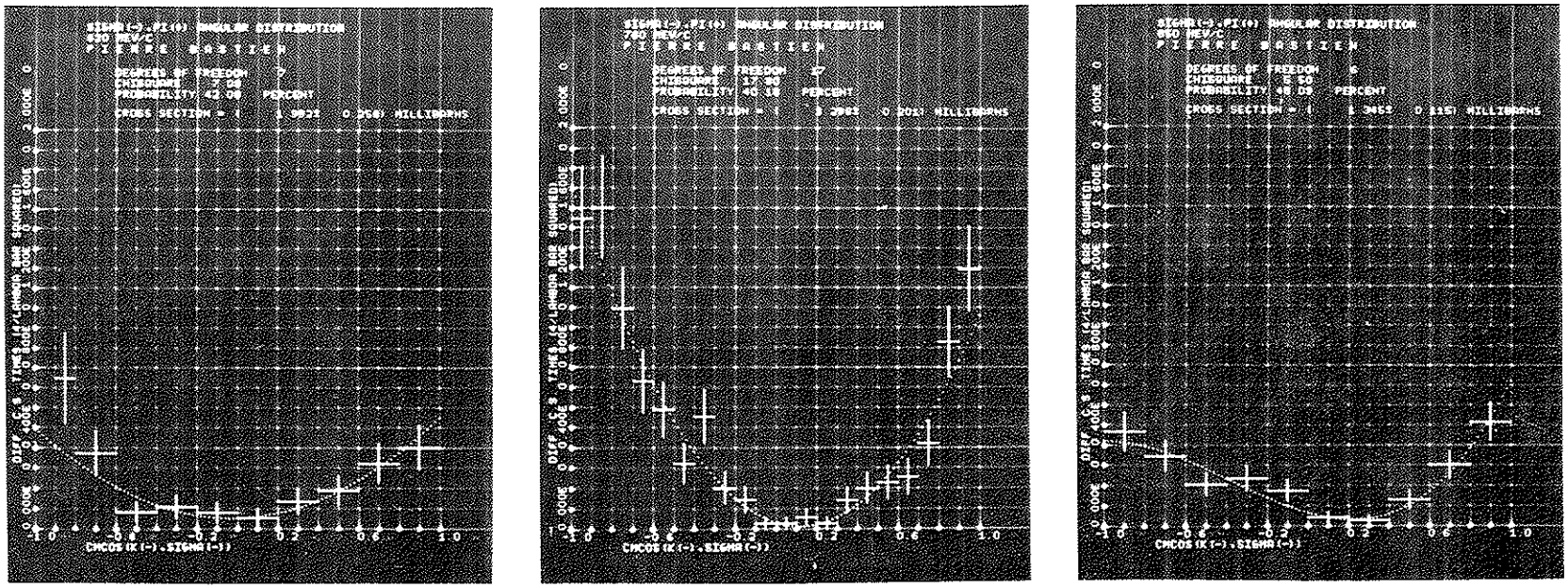

(a) (b) (c)

ZN-3797

Fig. 14. $K^- p \rightarrow \Sigma^- \pi^+$ angular distributions. The c.m. cosine is defined as $\hat{K}^-_{inc} \cdot \hat{\Sigma}^-$. We have (a) 620 MeV/c, (b) 760 MeV/c, and (c) 850 MeV/c.

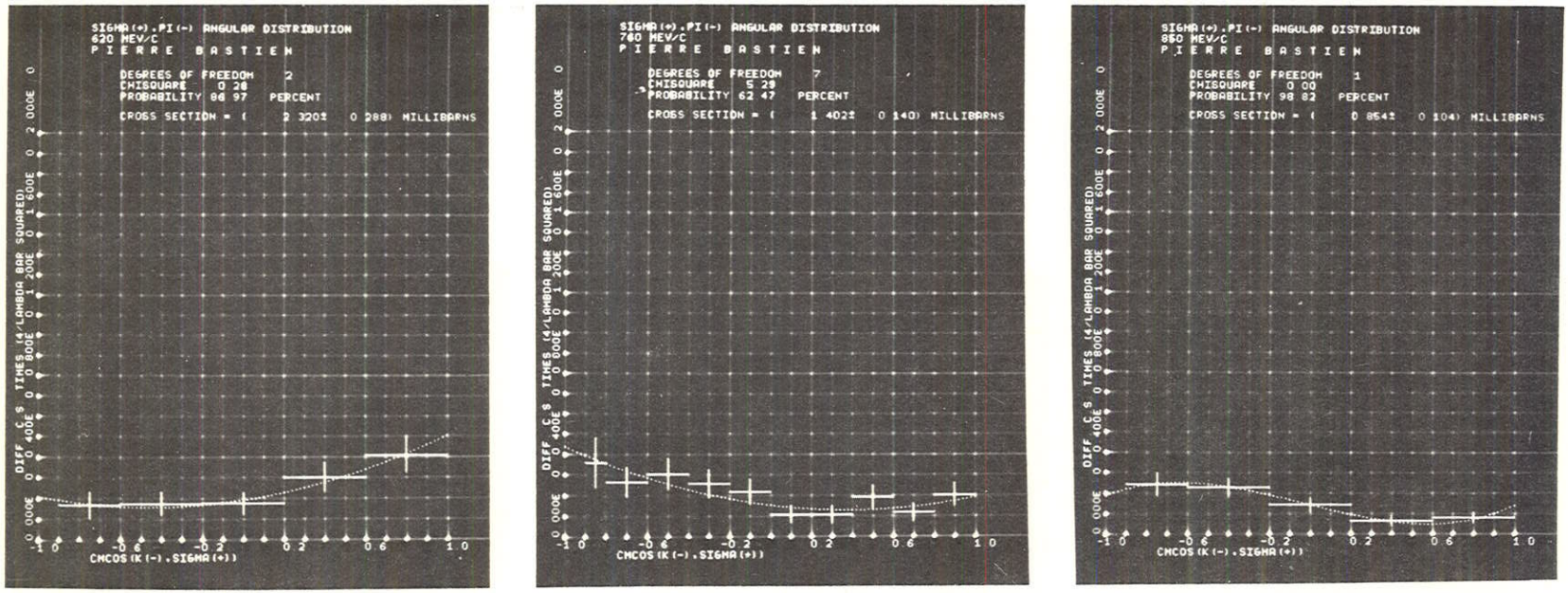

(a) (b) (c)

ZN-3798

Fig. 15. $K^- p \rightarrow \Sigma^+ \pi^-$ angular distributions. The c.m. cosine is defined as $\hat{K}^-_{inc} \cdot \hat{\Sigma}^+$. We have (a) 620 MeV/c, (b) 760 MeV/c, and (c) 850 MeV/c.

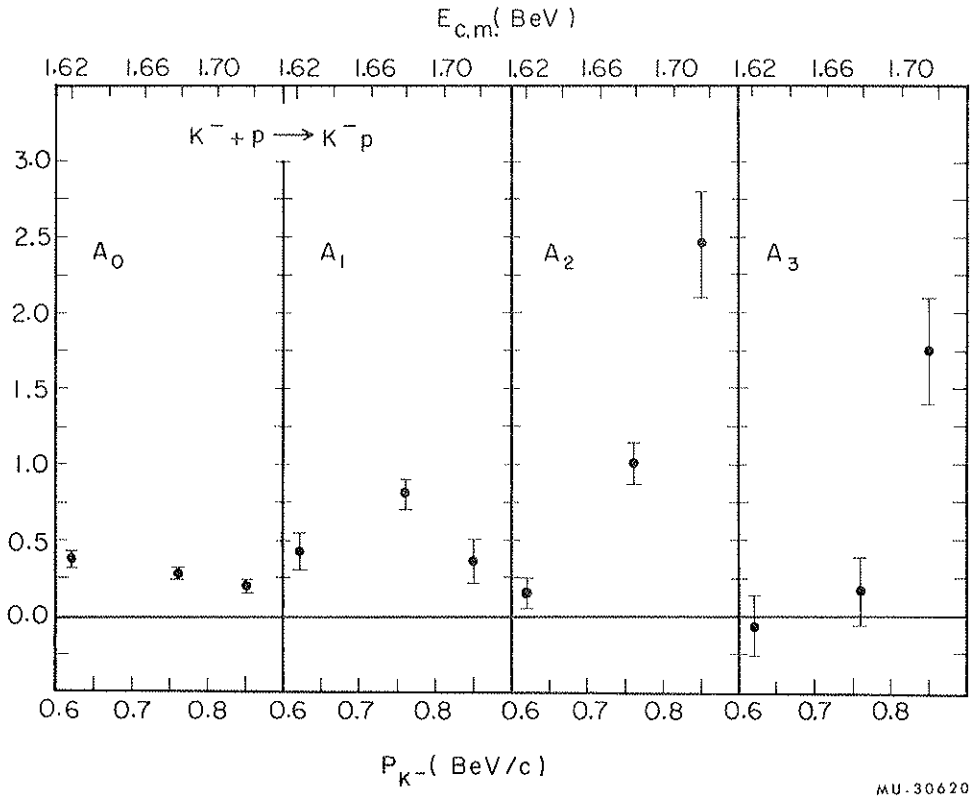

Fig. 16. Values of the coefficients A_l as a function of energy for $K^-p \to K^-p$ with the angular distributions fitted to order 3. The normalization used for the A_l is given in Eq. (III-14).

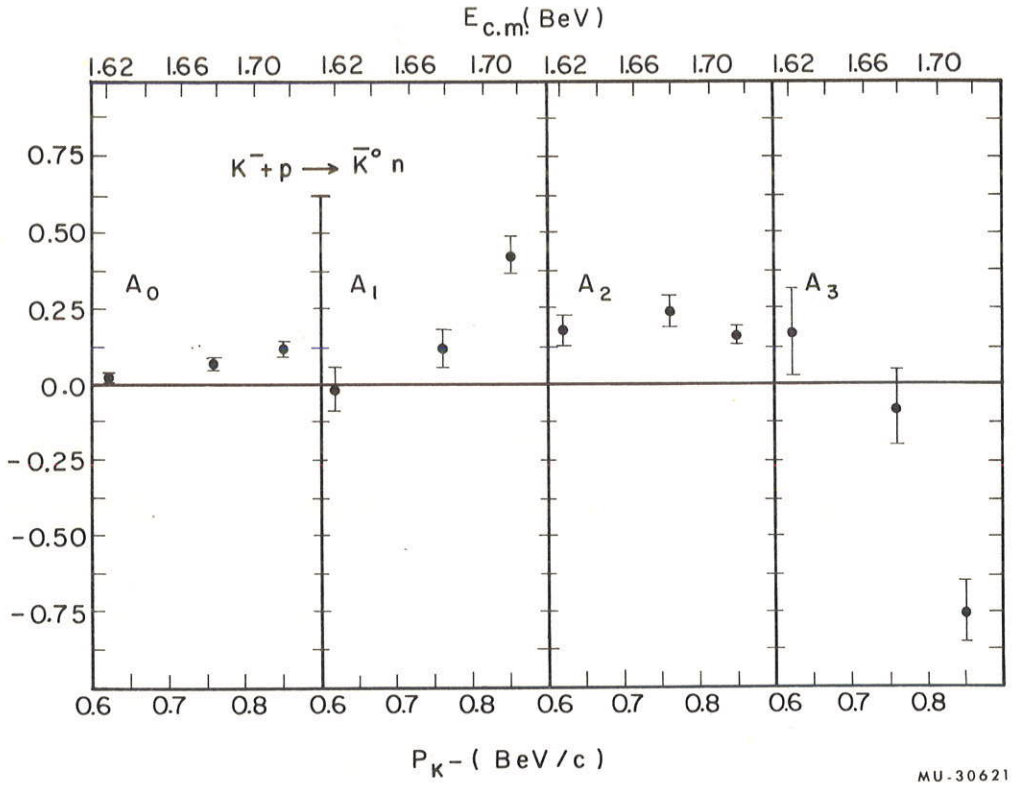

Fig. 17. Values of the coefficients A_i as a function of energy for $K^- p \rightarrow \overline{K}^0 n$ with the angular distributions fitted to order 3. The normalization used for the A_i is given in Eq. (III-14).

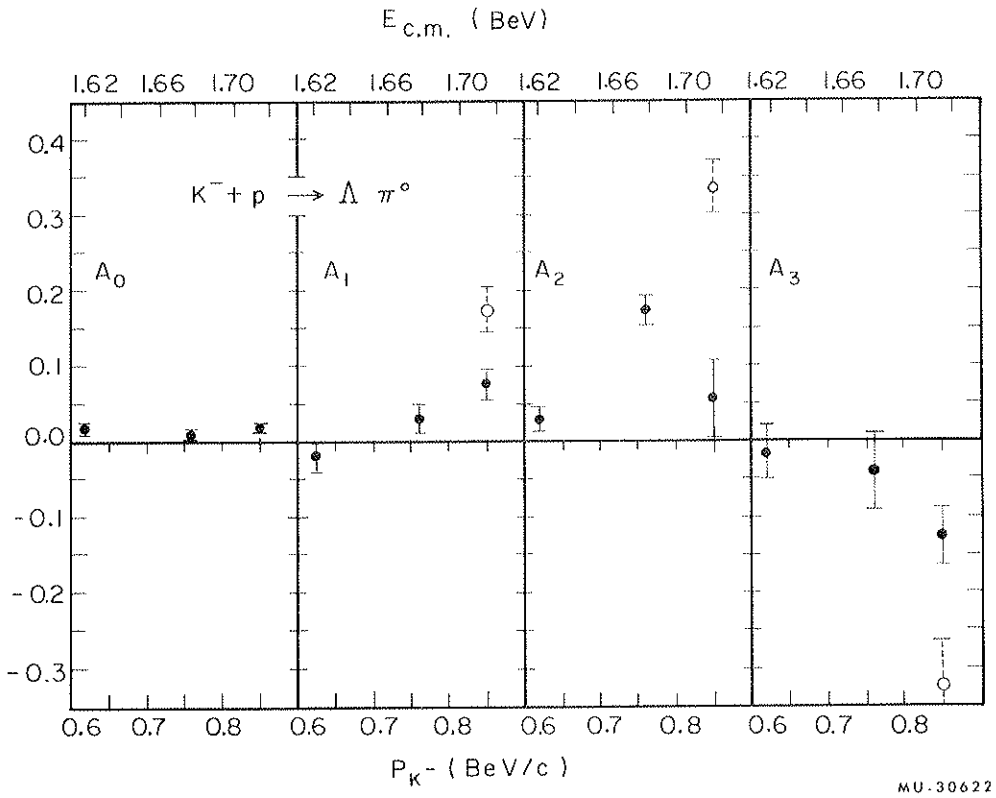

Fig. 18. Values of the coefficients A_l as a function of energy for $K^- p \to \Lambda \pi^0$ with the angular distributions fitted to order 3. The normalization used for the A_l is given in Eq. (III-14). At 850 MeV/c the dashed lines show the values of the coefficients when fitting to order 3, and the solid lines when fitting up to order 4. The value of A_4 in this last fit (not shown) is 0.16 ± 0.085.

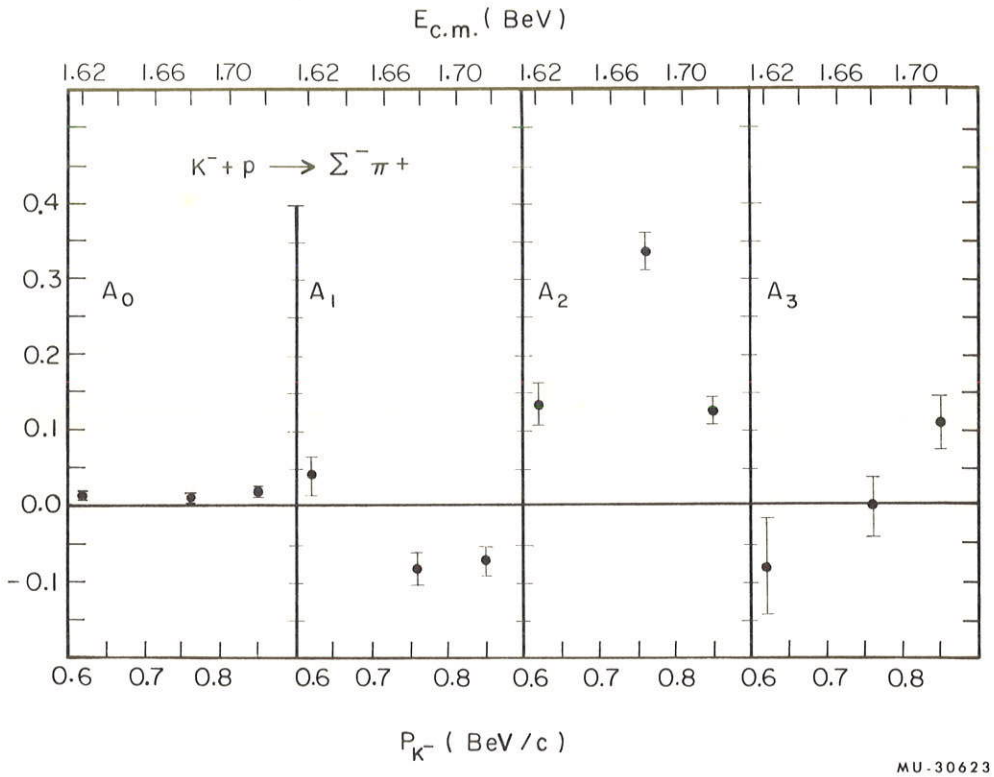

Fig. 19. Values of the coefficients A_i as a function of energy for $K^- p \rightarrow \Sigma^- \pi^+$ with the angular distributions fitted to order 3. The normalization used for the A_i is given in Eq. (III-14).

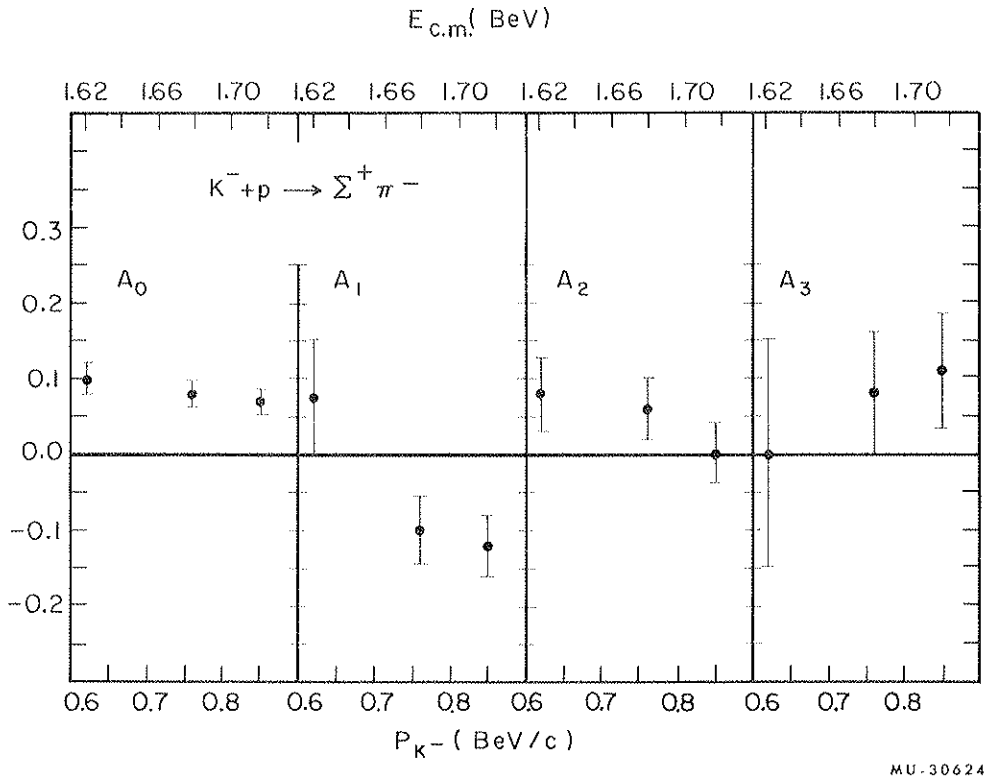

Fig. 20. Values of the coefficients A_i as a function of energy for $K^-p \to \Sigma^+\pi^-$ with the angular distributions fitted to order 3. The normalization used for the A_i is given in Eq. (III-14).

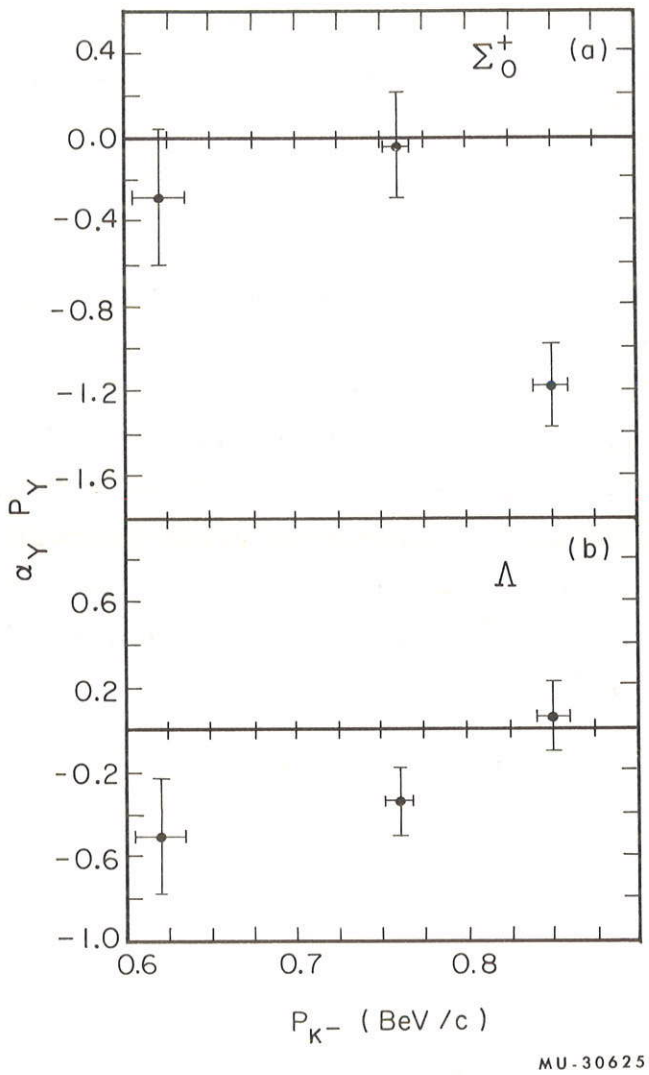

Fig. 21. Values of $\alpha_Y \overline{P}_Y$ for (a) $K^- p \rightarrow \Sigma_0^+ \pi^-$ and (b) $K^- p \rightarrow \Lambda \pi^0$. The subscript Y represents the hyperon. The sign conventions are given in Eq. (III-19).

have been plotted. We define the polarization of the hyperon as

$$\alpha_Y \overline{P}_Y = 2 \frac{N_{up} - N_{down}}{N_{up} + N_{down}} , \qquad \text{(III-18)}$$

where N_{up} represents the number of protons decaying from the hyperon Y such that

$$0 < \frac{\vec{K} \times \vec{Y}}{|\vec{K} \times \vec{Y}|} \cdot \frac{\vec{p}}{|\vec{p}|} < 1 . \qquad \text{(III-19)}$$

In the last formula, $\vec{p}$ represents the decay proton in the hyperon rest frame.

The large bias that we have mentioned for Σ_0^+ events affects production angular distributions, but not up-down asymmetries.

The cross sections for the three-body final states were obtained by adding the numbers of events properly weighted. All the cross sections are shown in Figs. 22 through 24, except those corresponding to $\overline{K}N\pi$ final states. A complete list of the cross sections is given in Table III.

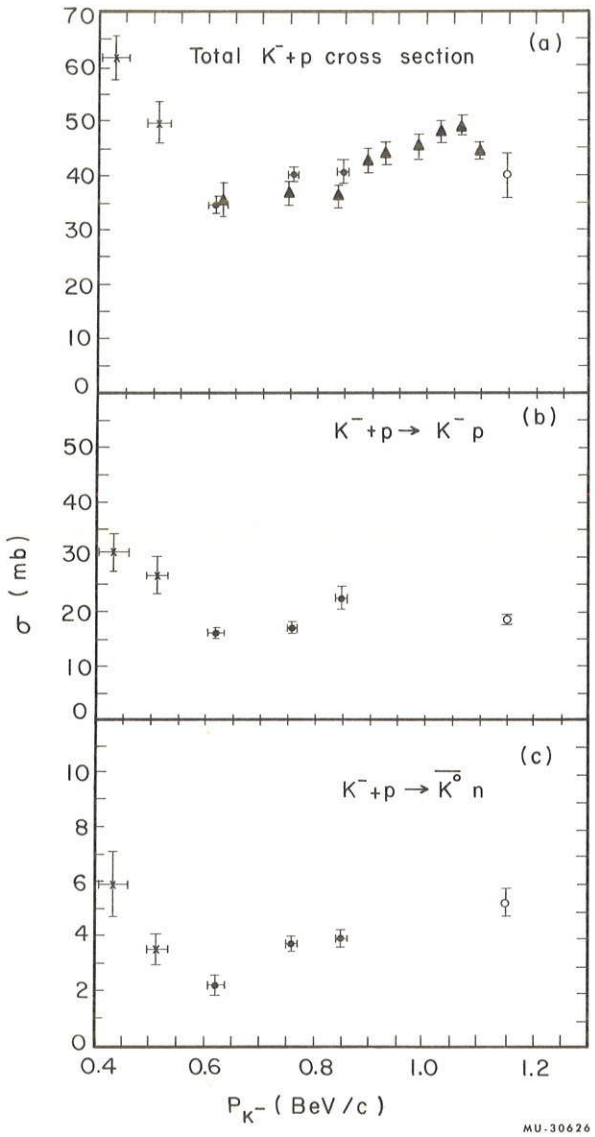

Fig. 22. (a) Total cross section for K^-p processes: "x" are the data of reference 8, ▲ the data of reference 21, ◯ the data of reference 3, and ● our data. (b) $K^-p \rightarrow K^-p$ cross section, and (c) $K^-p \rightarrow \overline{K}^0 n$ cross section.

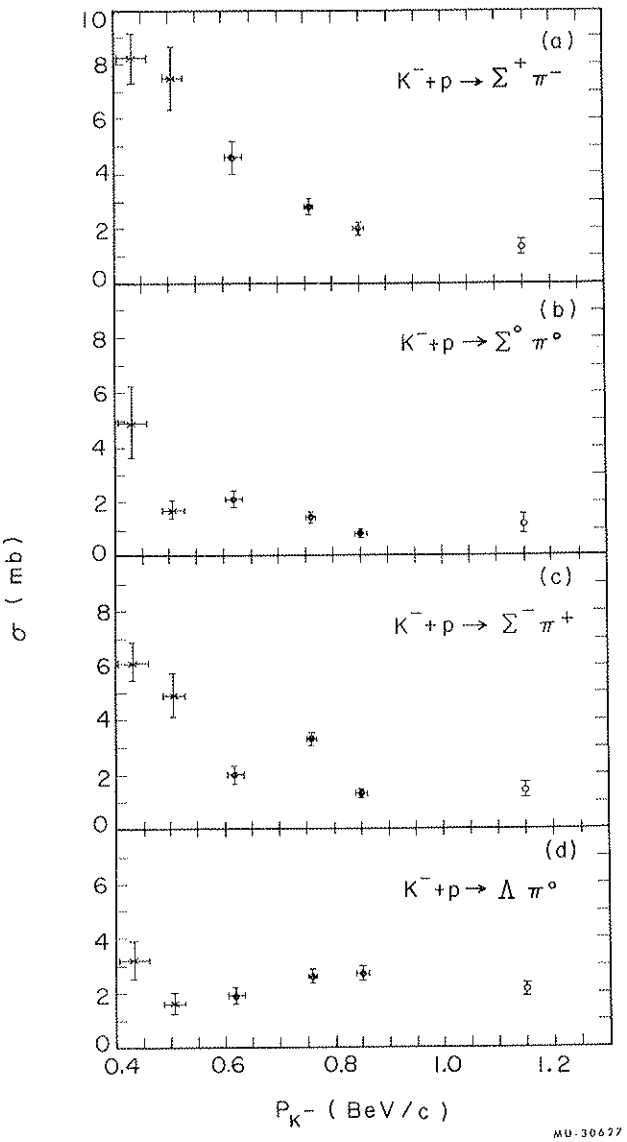

Fig. 23. Cross sections for K^-p going to (a) $\Sigma^+\pi^-$, (b) $\Sigma^0\pi^0$, (c) $\Sigma^-\pi^+$, and (d) $\Lambda\pi^0$. Points "x" are the data of reference 8, ◯ the data of reference 3.

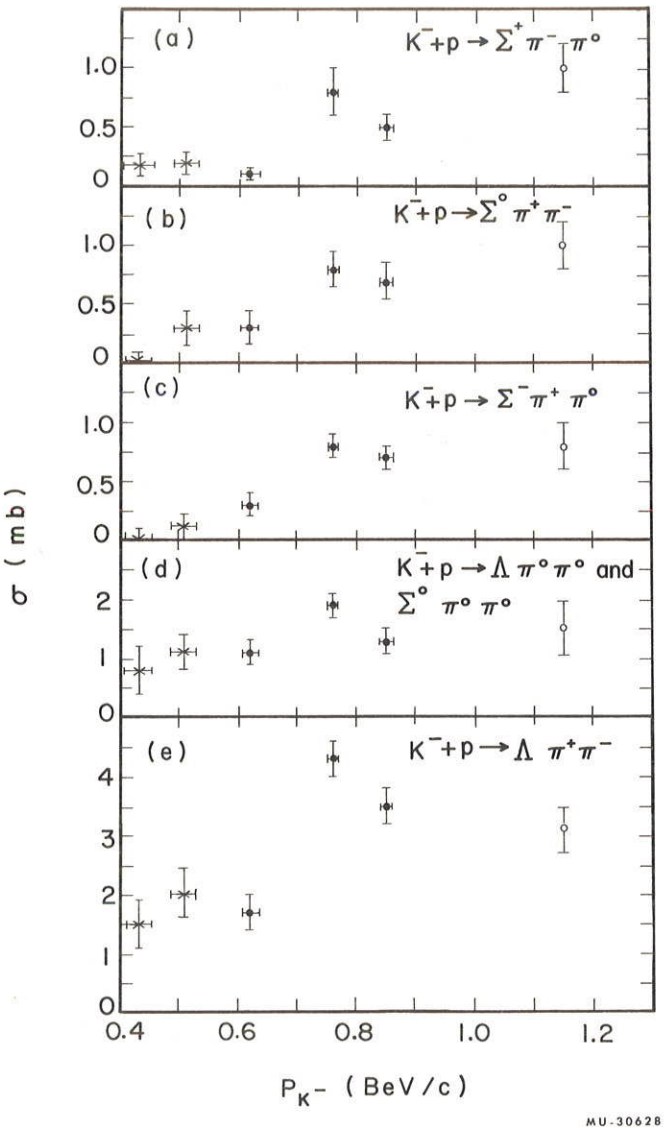

Fig. 24. Cross sections for K^-p going to (a) $\Sigma^+\pi^-\pi^0$, (b) $\Sigma^0\pi^+\pi^-$, (c) $\Sigma^-\pi^+\pi^0$, (d) $\Lambda\pi^0\pi^0 + \Sigma^0\pi^0\pi^0$, and (e) $\Lambda\pi^+\pi^-$. Points "x" are the data of reference 8, ◯ the data of reference 3.

Table III. Total cross sections in millibarns.[a]

Reaction	Topology[b]	P_{K^-} (MeV/c)	620±15	760±7	850±10
		$E_{c.m.}$ (MeV)	1616	1680	1723
			50 events/mb	124 events/mb	145 events/mb
K^-p	2-prong		16.0±1.0	16.7±1.0	22.4±2.0
$\bar{K}^0n$	0-prong + V		2.3±0.4	3.8±0.3	4.0±0.3
$\Sigma^+\pi^-$	2-prong (+ decays)[c]		4.6±0.6	2.8±0.3	2.0±0.2
$\Sigma^-\pi^+$	2-prong (- decays)		2.0±0.3	3.3±0.2	1.3±0.1
$\Sigma^0\pi^0$	0-prong + V		2.1±0.3	1.4±0.2	0.8±0.1
$\Lambda\pi^0$	0-prong + V		1.9±0.3	2.6±0.2	2.7±0.2
$\Lambda\pi^+\pi^-$	2-prong + V		1.7±0.3	4.3±0.3	3.5±0.3
$\Sigma^0\pi^+\pi^-$	2-prong + V		0.3±0.15	0.8±0.15	0.7±0.15
$\Sigma^-\pi^+\pi^0$	2-prong (-decays)		0.3±0.1	0.8±0.1	0.7±0.1
$\Sigma^+\pi^-\pi^0$	2-prong (+ decays)		0.1±0.5	0.8±0.2	0.5±0.1
$(\Lambda\Sigma^0)\pi^0\pi^0$	0-prong + V		1.1±0.2	1.9±0.2	1.3±0.2
$\Lambda\eta(\eta\to\text{neut})$	0-prong + V		—	0.5±0.15	0.15±0.1
$\Lambda\pi^+\pi^-\pi^0$	2-prong + V		0.0±0.03	0.25±0.05	0.15±0.05
$\bar{K}^0p\pi^-$	2-prong + V		0.0±0.03	0.04±0.03	0.10±0.06
$K^-p\pi^0$	2-prong		0.0±0.03	0.15±0.1	0.3±0.1
$K^-\pi^+n$	2-prong		0.06±0.06	0.0±0.05	0.2±0.1
$\bar{K}^0n\pi^0$	0-prong + V		0.0±0.03	0.0±0.05	0.3±0.1
Total			32.4±1.5	40.1±1.3	41.1±2.1
$(\Sigma\pi)_{I=0}$			6.4±0.8	4.2±0.5	2.3±0.3
$(\Sigma\pi)_{I=1}$			2.3±0.8	3.3±0.4	1.3±0.3
$\pi\lambda^2$			9.50	6.80	5.75

a. From reference 7.

b. Topological appearance of the event in the bubble chamber.

c. This means 2-prong, with decay of the + prong.

IV. INTERPRETATION OF THE RESULTS

In this section it is shown, on the basis of the cross sections and angular distributions just presented, that the $Y_1^*(1660)$ is being produced in this region. Also, what spin value of $Y_1^*(1660)$ is most consistent with our data is examined. Finally, the main features of the K^--p system at our energies are discussed.

The existence of a resonance around 1660 MeV was first suggested by Alexander et al.[5] and then definitively confirmed by Alvarez et al.[6] In this last experiment the resonance was produced in K^--p interactions at 1.51 BeV/c in the reaction

$$K^- + p \rightarrow Y_1^*(1660) + \pi \,. \qquad \text{(IV-1)}$$

In the experiment of Alvarez et al. the $Y_1^*(1660)$ was found to have the following properties:

Mass $E^R = 1660 \pm 10$ MeV.

Full width $\Gamma = 40 \pm 10$ MeV.

I spin $I = 1$.

The decay modes were $\Lambda\pi$, $\Sigma\pi$, $\Lambda\pi\pi$, $\Sigma\pi\pi$, and $\bar{K}N$, with the relative decay rates 7:6:4:4:<1. No statement could be made about the spin or parity on the basis of their data.

In our experiment the $Y_1^*(1660)$ cannot be produced together with a pion, but instead must be formed by the initial K^--p system. (see Fig. 31). It is then expected to decay into the various modes listed in the previous paragraph.

In Fig. 25 is shown a plot of the total energy in the center-of-mass system vs the beam momentum in our region. The data points, and their positions with respect to the central value and width quoted by Alvarez et al. for the resonance, also appear on the plot. At 760 MeV/c we are only a half-width above the central value of $Y_1^*(1660)$, and therefore expect the resonance to be formed, at that momentum, in the reactions

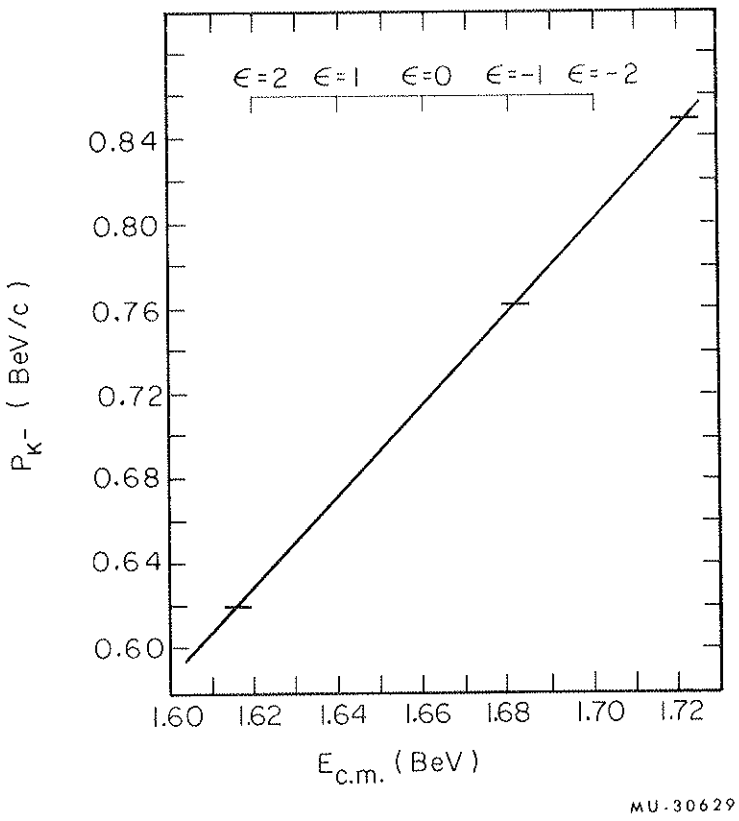

Fig. 25. Beam momentum as a function of the energy in the center-of-mass system. Our three data points are represented as horizontal bars crossing the curve. The scale at the top represents the central value and width of $Y_1^*(1660)$, as given in reference 6, as a function of the quantity $\epsilon = 2(E^R - E_{c.m.})/\Gamma$.

$$K^- + p \rightarrow Y_1^*(1660) \rightarrow \bar{K}N \ (K^-p, \bar{K}^0n), \qquad \text{(IV-2)}$$

$$K^- + p \rightarrow Y_1^*(1660) \rightarrow \Sigma\pi \ (\Sigma^-\pi^+, \Sigma^+\pi^-), \qquad \text{(IV-3)}$$

$$K^- + p \rightarrow Y_1^*(1660) \rightarrow \Lambda\pi \ (\Lambda\pi^0), \qquad \text{(IV-4)}$$

$$K^- + p \rightarrow Y_1^*(1660) \rightarrow \Lambda\pi\pi(\Lambda\pi^+\pi^-), \qquad \text{(IV-5)}$$

$$K^- + p \rightarrow Y_1^*(1660) \rightarrow \Sigma\pi\pi(\Sigma^-\pi^+\pi^0, \Sigma^+\pi^-\pi^0, \Sigma^0\pi^+\pi^-, \Sigma^0\pi^0\pi^0) \qquad \text{(IV-6)}$$

As seen in a following section, the resonance is indeed clearly observed in some of these cross sections.

The discussion is divided into three parts:

(a) The data are analyzed according to the assumption that the resonance is adequately described by a Breit-Wigner resonance, and the effects of such a resonant form on cross sections are discussed.

(b) It is shown that $Y_1^*(1660)$ is produced in the region.

(c) The spin of the resonance is discussed. The arguments to rule out spin 1/2 are based on the behavior of the cross sections. To distinguish between spin values $> 1/2$, the energy dependence of the angular distributions throughout the region is examined.

A. Breit-Wigner Resonances

In general, the cross section for a state of definite total angular momentum J and orbital angular momentum ℓ is given by[22]

$$\sigma^{J,\ell}(k \rightarrow j) = 4\pi\lambda^2\left(J+\tfrac{1}{2}\right) \left| T^{J,\ell}(k \rightarrow j)\right|^2, \qquad \text{(IV-7)}$$

where $T^{J,\ell}(k \rightarrow j)$ is the amplitude for channel k going to channel j (subscript k will be used to denote the incident channel from this point on). The overall cross section for $k \rightarrow j$ is given by

$$\sigma(k \rightarrow j) = \sum_J \left\{\sigma^{J,J-1/2}(k \rightarrow j) + \sigma^{J,J+1/2}(k \rightarrow j)\right\}. \qquad \text{(IV-8)}$$

Since the amplitudes usually have small energy dependences, the nonresonant cross sections of Eq. (IV-8) vary slowly as a function of energy.

Breit and Wigner have shown that when a multichannel resonance of given total angular momentum and parity is present, the corresponding amplitude takes the form

$$T_R^{J,\ell}(k\to j) = \frac{\sqrt{x_k x_j}}{\epsilon - i} \quad . \tag{IV-9}$$

The normalized partial widths x_j are defined as Γ_j/Γ, the ratio of the partial width Γ_j to the full width Γ. The dimensionless Breit-Wigner parameter ϵ is defined as $2(E^R - E_{c.m.})/\Gamma$, where E^R is the resonance energy and $E_{c.m.}$ the total energy in the center-of-mass system. The cross section corresponding to this amplitude is

$$\sigma_R^{J,\ell}(k\to j) = 4\pi\lambda^2 \left(J + \frac{1}{2}\right) \frac{x_k x_j}{\epsilon^2 + 1} \quad . \tag{IV-10}$$

This leads immediately to the elastic, inelastic, and total cross sections, due to the resonance,

$$\sigma_R^{J,\ell,\,\text{elastic}} = 4\pi\lambda^2 \left(J + \frac{1}{2}\right) \frac{x_k^2}{\epsilon^2 + 1} \quad , \tag{IV-11}$$

$$\sigma_R^{J,\ell,\,\text{inelastic}} = 4\pi\lambda^2 \left(J + \frac{1}{2}\right) \frac{x_k(1 - x_k)}{\epsilon^2 + 1} \quad , \tag{IV-12}$$

$$\sigma_R^{J,\ell,\,\text{total}} = 4\pi\lambda^2 \left(J + \frac{1}{2}\right) \frac{x_k}{\epsilon^2 + 1} \quad . \tag{IV-13}$$

The cross sections $\sigma(k\to j)$ of Eq. (IV-8), when a resonance is present, therefore appear as the bell-shaped curve of Eq. (IV-10) superimposed on the slowly varying background. The knowledge of the $\sigma(k\to j)$ for all channels as a function of energy is therefore, in principle, sufficient to determine all the normalized partial widths x_j, and the spin J.

From Eqs. (IV-11) through (IV-13) we see that a knowledge of the total resonant cross section is sufficient to determine both elastic and inelastic resonant cross sections, since the total resonant cross section determines x_k. This is one of the internal consistency checks that are possible when the Breit-Wigner formula is used. These checks

cannot be made in this experiment, because we have too few data points in the region. However, let us assume that the Breit-Wigner formula is applicable to our case, since it has led to perfectly consistent results in the analysis of several resonances of elementary-particle physics: $N^*_{3/2}$ (1238), $N^*_{1/2}$ (1515), $N^*_{1/2}$ (1688), and recently Y^*_0 (1520).[4,6,8]

The formulas given above for the cross sections are complicated by the fact that the K^--p system is not in a pure I-spin state. In general, the amplitude $T^{J,\ell}(k \to j)$ for a state of given J and ℓ is a sum of pure $I = 0$ and $I = 1$ amplitudes, each of them being multiplied by appropriate Clebsch-Gordan coefficients. Namely, we have

$$T^{J,\ell}(k \to j) = C_0 T_0^{J,\ell}(k \to j) + C_1 T_1^{J,\ell}(k \to j), \qquad \text{(IV-14)}$$

where C_0 and C_1 are the Clebsch-Gordan coefficients for I spin = 0 and =1 (see Appendix A). Therefore, the cross sections $\sigma^{J,\ell}(k \to j)$ of Eq. (IV-7) contain interference terms. In particular, if one of the amplitudes of Eq. (IV-14) is resonant, all the formulas given in Eq. (IV-10) through (IV-13) must be modified to account for the interference terms. However, as is shown in Appendix B, the sum of the cross sections for the charge states of a given channel is free of interferences. For instance, the sum of the cross sections for $K^- p \to \Sigma^+ \pi^-$, $\Sigma^0 \pi^0$, and $\Sigma^- \pi^+$ does not contain any interferences. When the sums are used, Eqs. (IV-10) through (IV-13) are strictly correct provided the I spin is further specified and provided they are all multiplied by a factor of 1/2 to take care of the I-spin decomposition of the initial state. Because of this we mean from this point on, by elastic cross section, the sum of the K^-p and $\bar{K}^0 n$ channels.

The effects of a resonance on angular distributions are more complicated, since they depend on interferences with the nonresonant amplitudes. The problem is examined below (Sec. IV. C.1).

B. Existence of $Y_1^*(1660)$

In Fig. 26 we have plotted the elastic cross section, namely, the sum of the K^--p and the $\bar{K}^0$n channels, and no bump is observed. However, the inelastic cross section plotted in Fig. 27 shows a clear bump of approximately 6 mb at 760 MeV/c, where the $Y_1^*(1660)$ is expected to appear.

Before drawing any conclusions on this effect we must determine which channels are responsible for the rise and what their I spin is. If the effect is due to $Y_1^*(1660)$ I spin 1 is, of course, expected on the basis of the results of Alvarez et al. We will therefore examine the cross sections for the inelastic channels one by one. These cross sections are plotted in Figs. 23 and 24, and given in Table III.

The $\Lambda\eta$ final state is below threshold at 620 MeV/c; it has a cross section of 0.7 mb at 760 MeV/c, and approx 0.2 mb at 850 MeV/c. The η has I spin 0 and the $\Lambda\eta$ channel is therefore I spin 0. However, this can contribute only 0.5 mb to the bump.

In the $\Sigma\pi$ channel we notice a clear bump in the cross section for the $\Sigma^-\pi^+$ charge state (Fig. 23). To determine the I spin of the bump, we can decompose the $\Sigma\pi$ cross sections into I spin 0 and I spin 1, using the formulas

$$\sigma(\Sigma\pi;\ I=0) = 3\sigma(\Sigma^0\pi^0)\ , \tag{IV-15}$$

and

$$\sigma(\Sigma\pi;\ I=1) = \sigma(\Sigma^+\pi^-) + \sigma(\Sigma^-\pi^+) - 2\sigma(\Sigma^0\pi^0)\ . \tag{IV-16}$$

The results of this separation have been plotted in Fig. 28. It is clear that the I-spin-1 part of the amplitude is responsible for the bump. The I spin 1 bump in $\Sigma\pi$ is estimated to be 1.75 ± 0.5 mb.

Let us now examine the $\Lambda\pi\pi$ channel. There are two possible charge states: $\Lambda\pi^+\pi^-$ and $\Lambda\pi^0\pi^0$. The $\Lambda\pi^+\pi^-$ is a combination of I spin 0 and I spin 1 but does not contain any interferences between

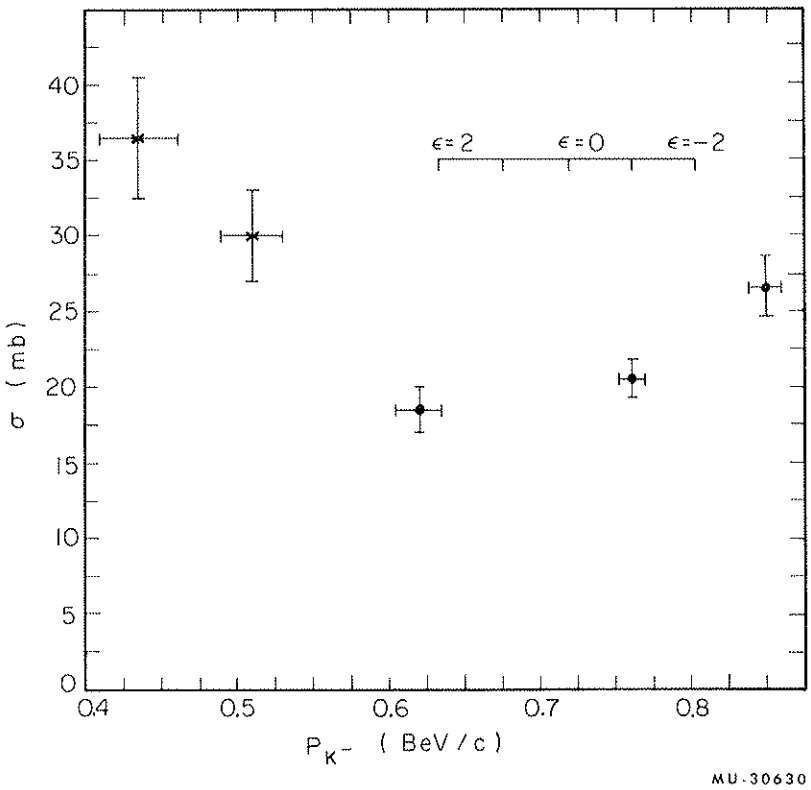

Fig. 26. Sum of the K^-p and $\bar{K}^0n$ cross sections as a function of energy.

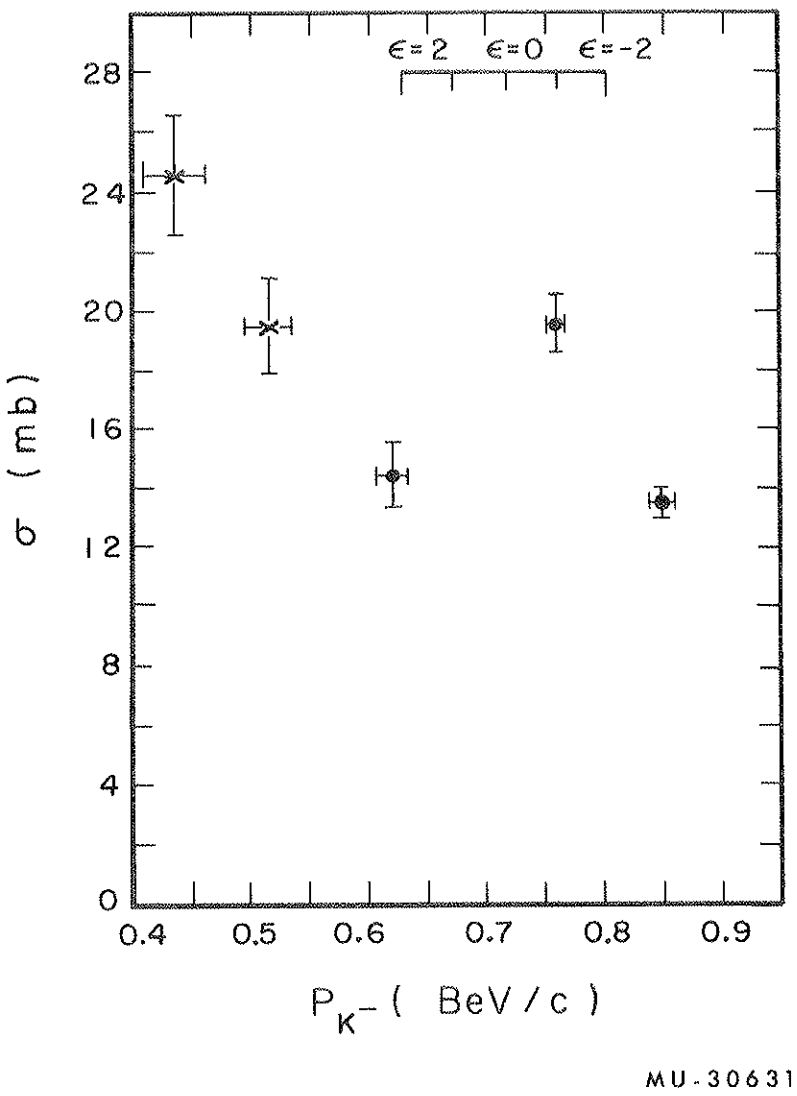

Fig. 27. Sum of the cross sections for inelastic processes except the $\bar{K}N\pi$ channels. The bump at 760 MeV/c is attributed to $Y_1^*(1660)$.

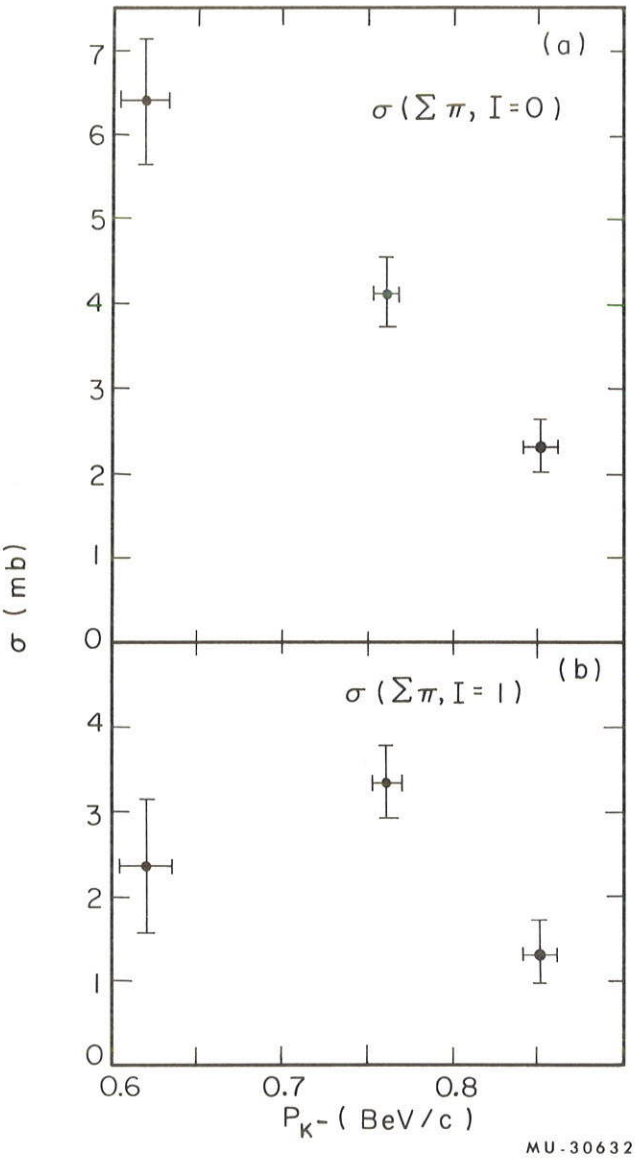

Fig. 28. (a) The pure I = 0 $\Sigma\pi$ cross section, as defined in Eq. (IV-15).
(b) The pure I = 1 $\Sigma\pi$ cross section, as defined in Eq. (IV-16).

these two states in total rates, i.e., if we integrate over all $\pi^+\pi^-$ angles. Examining first the behavior of the $\Lambda\pi^+\pi^-$ cross section plotted on Fig. 24, we see a bump at 760 MeV/c. It is impossible to determine the I spin of this bump without a knowledge of the behavior of the $\Lambda\pi^0\pi^0$ cross section. Indeed, the $\Lambda\pi^0\pi^0$ channel is pure I spin 0, and should not show any effect if the bump in $\Lambda\pi^+\pi^-$ is in I spin 1. Unfortunately $\Lambda\pi^0\pi^0$ events cannot be separated from $\Sigma\pi^0\pi^0$ events in our experiment. However, indirect information on the behavior of the I = 0 part of the $\Lambda\pi\pi$ channel is available. An experiment in deuterium at the same energies as ours has given data on the ratio[23]

$$r = \frac{K^- n \to \Lambda\pi^0\pi^-}{K^- p \to \Lambda\pi^+\pi^-} = \frac{2\left|T_1(\bar{K}N \to \Lambda\pi\pi)\right|^2}{\left|T_1(\bar{K}N \to \Lambda\pi\pi)\right|^2 + \left|T_0(\bar{K}N \to \Lambda\pi\pi)\right|^2} \quad \text{(IV-17)}$$

With the knowledge of that ratio, and of the $\Lambda\pi^+\pi^-$ cross section, it is possible to calculate the $\Lambda\pi^0\pi^0$ cross section as a function of energy. The results are listed in Table IV, and it can be seen that the $\Lambda\pi^0\pi^0$ cross section is small throughout. Because of the large errors it is not possible to tell whether a bump is present or not. In conclusion, an effect of approximately 1.25 ± 0.4 mb is observed in $\Lambda\pi^+\pi^-$, but its I spin cannot be determined.

Going now to the $\Sigma\pi\pi$ channel, we have plotted in Fig. 29 the sum of the four $\Sigma\pi\pi$ cross sections; this sum is free of interferences. The curve shows a bump of approx 2.0 ± 0.5 mb at 760 MeV/c. Since the $\Lambda\pi^0\pi^0$ cannot be separated from the $\Sigma^0\pi^0\pi^0$, as we have just mentioned, the former are also included in Fig. 29. But we have established that the $\Lambda\pi^0\pi^0$ cross section is small and could not possibly account for an effect of that size. The I spin of the effect cannot be established.

Finally, in the $\Lambda\pi^0$ channel, which is pure I spin 1, no effects are observed in cross sections (see Fig. 23). The coefficient of the $\cos^2\theta$ term in the angular distribution for that channel shows a bump

Table IV. Cross section for $\Lambda\pi^0\pi^0$

	p_{K^-}(MeV/c)		
	620	760	850
r^a	1.0 ± 0.4	1.4 ± 0.3	2.0 ± 0.3
$\sigma(\Lambda\pi^0\pi^0)$ (mb)	0.4 ± 0.3	0.6 ± 0.5	0.0 ± 0.5
$\sigma(\Sigma^0\pi^0\pi^0)$ (mb)	0.7 ± 0.3	1.4 ± 0.5	1.1 ± 0.5

a. This quantity is defined in Eq. (IV-17)

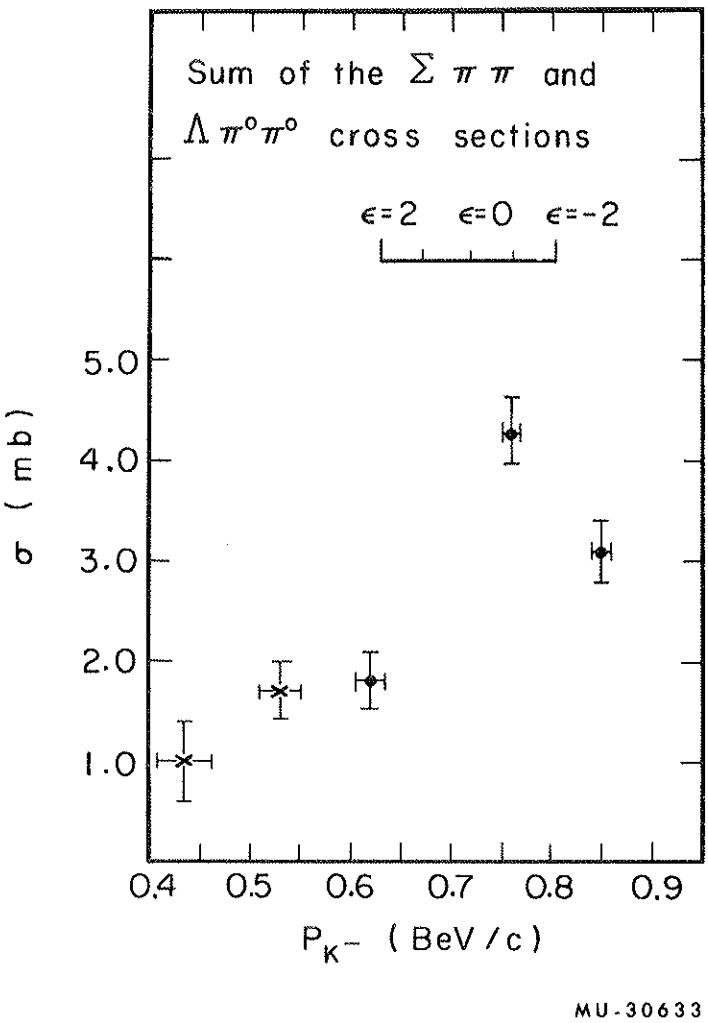

Fig. 29. Sum of the $\Sigma\pi\pi$ cross sections. The $\Lambda\pi^0\pi^0$, which cannot be separated from $\Sigma^0\pi^0\pi^0$, are also included.

at 760 MeV/c (see Fig. 18). This bump is quite probably due to an interference between a small resonant amplitude and the background, as is explained below. Nevertheless, in this channel, the resonant cross section is consistent with zero, and is in any case smaller than 0.5 mb.

To summarize what has been discussed up to this point, it is clear that there is a bump in the inelastic cross section at the momentum where we expect to form $Y_1^*(1660)$. It is clear that the $\Sigma\pi$, $\Lambda\pi\pi$, and $\Sigma\pi\pi$ channels are responsible for the observed bump. We have established that the $\Sigma\pi$ channel effect is in I spin 1. We conclude that the only reasonable interpretation of these phenomena is that $Y_1^*(1660)$ is responsible for them.

C. Spin of $Y_1^*(1660)$

We examine first what can be said about the spin on the basis of the bump in the inelastic cross section. The angular distributions are then examined for further information.

1. Cross Sections and the Spin of $Y_1^*(1660)$

In this section we show that spin 1/2 for $Y_1^*(1660)$ is ruled out by the behavior of the cross sections. Then, we examine discrepancies between the branching ratios for the various channels in the experiment by Alvarez et al. and in ours.

There is no effect in the elastic cross section but there is a clear effect in the inelastic cross section. In Eq. (IV-12) we have written the resonant inelastic cross section. We want to examine the quantity $x_k(1-x_k) \equiv A$, which appears in Eq. (IV-12). As we have mentioned in connection with Eq. (IV-14), the formula given in Eq. (IV-12) for the inelastic cross section must be multiplied by 1/2 to take care of the I-spin decomposition of the initial state. The quantity A is therefore given, in our case, by

$$x_k(1-x_k) \equiv A = \frac{1}{2\pi\lambda^2} \cdot \frac{1}{J+1/2} \cdot \sigma_R^{in} \cdot (\epsilon^2+1) . \qquad \text{(IV-18)}$$

The dimensionless Breit-Wigner parameter, ϵ, defined below Eq. (IV-9), is equal to $(2/\Gamma)(E^R - E_{c.m.})$. The quantity A of Eq. (IV-18) clearly

cannot exceed 0.25, since x_k can vary only between 0 and 1. Therefore, given ϵ and σ_R^{in}, A may be greater than 0.25 for certain values of J. These values of J would therefore be unphysical and would be ruled out.

In order to see if A is greater than 0.25 for J = 1/2, we must know both σ_R^{in} and ϵ. Since we have only one data point in the resonance region we can determine neither the width, Γ, nor the central value, E^R, of $Y_1^*(1660)$. Consequently, we cannot calculate ϵ. However, we notice that A is a quadratic function of ϵ and therefore we can assume ϵ to be zero. Indeed, other things remaining equal, that value of ϵ gives the lower bound on A. The assumption that ϵ is equal to zero amounts to saying that the central value of the resonance is equal to the total energy in the c.m. at 760 MeV/c i.e., 1682 MeV. Using 5.0 ± 1.0 mb for σ_R^{in} and zero for ϵ, we find that A has the values 0.37 ± 0.072, for spin 1/2, 0.185 ± 0.036 for spin 3/2, and 0.123 ± 0.024 for spin 5/2. Whereas the values of A for spin 3/2 and 5/2 are smaller than 0.25, the value of A for spin 1/2 is not. The probability that 0.37 ± 0.072 is smaller than 0.25 is only 8.3%. We have displayed as dotted curves on Fig. 30 the probability of obtaining a given value of A, as a function of A, for spin 1/2, 3/2, and 5/2. The curves are Gaussians whose central values and widths have just been given above. The ratio of the area under the spin-1/2 dashed curve to the total area under the curve is 0.083. The probability of spin 1/2 is therefore 8.3%.

We now wish to take into account the information given by Alvarez et al. on the central value (1660 ± 10 MeV), and width (40 ± 10 MeV). We have found that the probability of finding spin 1/2 was 8.3%, under the assumption that the central value is 1682 MeV. But this value of 1682 MeV is itself two standard deviations away from the central value quoted by Alvarez et al. If we take this additional information into account it is clear that ϵ is most likely to be different from zero and that the probability for spin 1/2 must be even lower than 8.3%. We have made a complete error analysis using our value of σ_R^{in} and the Alvarez et al. values for the central value and width. The details of the analysis are discussed in Appendix C. The results for spin 1/2 are shown on Fig. 30a. We have again plotted in Fig. 30a as a solid curve the probability of finding a given value of A. By integrating this

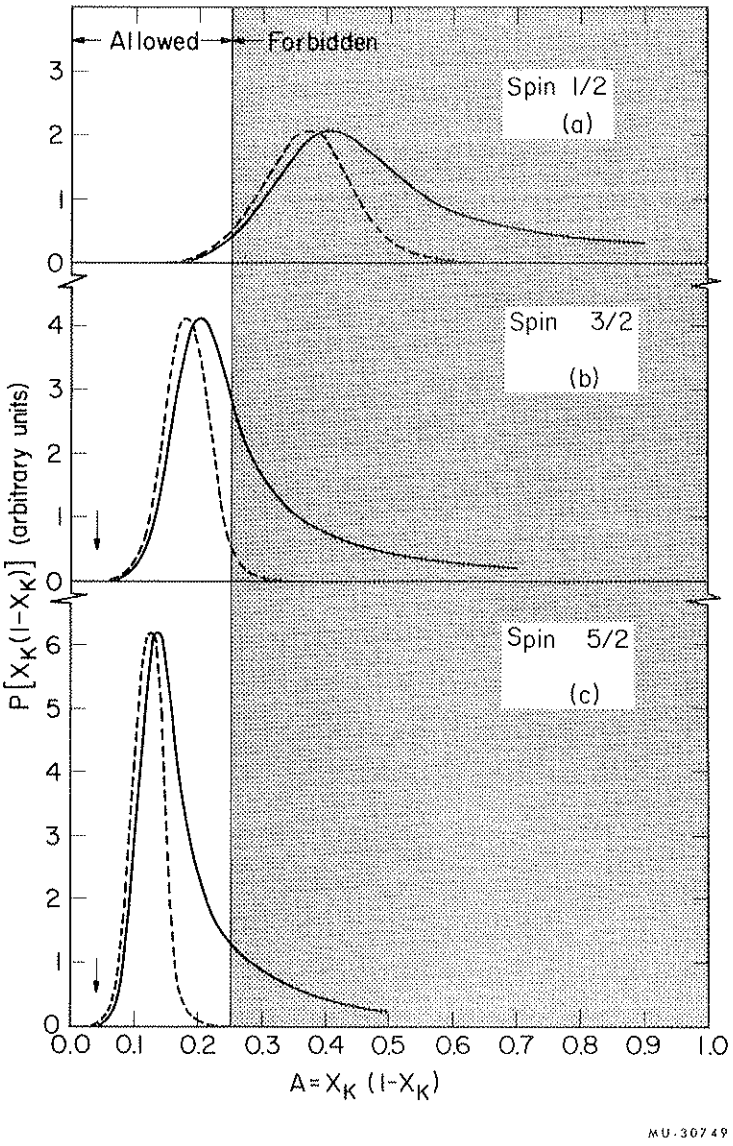

Fig. 30. Probability P(A) of obtaining a given value of $A \equiv x_k(1-x_k)$ as a function of $x_k(1-x_k)$ for spin 1/2, 3/2, and 5/2. The dashed curves are the probability functions for $\epsilon = 0$. The solid curves are the probability functions when the central value and width from Alvarez et al. are used to calculate ϵ. The dashed curves are Gaussian, whereas the solid curves are not. The calculation of the latter curves is explained in Appendix C.

curve over the allowed region ($0 < A < 0.25$) and dividing the result by the total area under the curve, we find that the probability of spin 1/2 is only 2.5%. We conclude that spin 1/2 is ruled out. A similar analysis has been performed for spin 3/2 and 5/2 and the results are shown on Figs. 30b and 30c. We find that both spin 3/2 and 5/2 are consistent with A's being smaller than 0.25.

We now want to find the lower and upper limits that we can set on the value of x_k itself using our experimental results. Alvarez et al. obtained an upper limit of 0.04 for x_k (see Table VI) and we want to see if our value for x_k is consistent with it. We will consider henceforth only spin 3/2 and 5/2. Using our value of σ_R^{in} and setting ϵ to zero, we have found that A, for spin 3/2, is 0.185 ± 0.036. This means that A has only a 2.5% probability of being smaller than 0.11, that is, two standard deviations below 0.185. We can now solve $A \equiv x_k(1-x_k)$ for x_k and we find that x_k has only a 2.5% probability of being smaller than 0.13 if the spin is 3/2. By the same calculation for spin 5/2 we find that x_k has a 2.5% probability of being smaller than 0.08.

We can now use the central value and width from Alvarez et al. and, with this additional information, again calculate the lowest possible values of x_k for spin 3/2 and spin 5/2. We find that x_k has 2.5% probability of being smaller than (a) 0.16 if the spin is 3/2, and (b) 0.09 if the spin is 5/2. Also, the most likely values of x_k and their errors for spin 3/2 and 5/2 can be found from Figs. 30b and 30c. For spin 3/2 we find $x_k = 0.28^{+0.22}_{-0.13}$ and $x_k = 0.72^{+0.13}_{-0.22}$. There are two most likely values of x_k because $A \equiv x_k(1-x_k)$ has two roots. The errors given serve merely as indications, since they are extremely skewed. For spin 5/2 we find $x_k = 0.18^{+0.08}_{-0.06}$ and $x_k = 0.82^{+0.06}_{-0.08}$. All these results are summarized in Table V.

We finally want to see what upper limit can be set on the value of x_k when we use the elastic cross section plotted on Fig. 26. No

Table V. Summary of the discussion on the limits imposed on the quantities A and x_k [a]

	Limits on A and x_k obtained by using data from this experiment alone [b]			Limits on A and x_k obtained by using data from this experiment and the Alvarez et al. experiment [c]			
Spin	A [d]	P(A < 0.25) [e]	x_k^{min} [f]	A [d]	P(A < 0.25) [e]	x_k^{min} [f]	x_k [g]
1/2	0.370±0.072	8.3%	—	$0.40^{+0.15}_{-0.10}$	2.5%	—	—
3/2	0.185±0.036	97.5%	0.13	$0.20^{+0.08}_{-0.04}$	50.0%	0.16	$0.28^{+0.22}_{-0.13}$ or $0.72^{+0.13}_{-0.22}$
5/2	0.123±0.024	100.0%	0.08	$0.14^{+0.06}_{-0.04}$	76.0%	0.09	$0.18^{+0.08}_{-0.06}$ or $0.82^{+0.06}_{-0.08}$

a. The reader is referred to Sec. IV. c. 1 for a complete discussion of this table.

b. The data used for these calculations were only the resonant inelastic cross section of our experiment (5.0±1.0 mb).

c. The data used for these calculations were the resonant inelastic cross section of our experiment together with the Alvarez et al. central value (1660±10 MeV) and width (40±10 MeV) for $Y_1^*(1660)$.

d. A is defined in Eq. (IV-18).

e. Probability (%) that A is smaller than 0.25, i.e., that A has physical value.

f. x_k^{min} is defined as follows: there is a 2.5% probability that the true value of x_k is smaller than x_k^{min}.

g. Most likely value of x_k and its error. There are two values of x_k, since it is computed from $x_k(1-x_k)$, which has two roots.

bump is observed at 760 MeV/c in the elastic cross section. However, we feel that as much as 8 to 10 mb of that cross section could be due to $Y_1^*(1660)$. Indeed, it is possible that some structure at 760 MeV/c is hidden by the behavior of the 850-MeV/c point, which is on the rising edge of the Kerth bump.[21] The ratio of the elastic to inelastic cross sections is equal to $x_k/(1-x_k)$ and is spin-independent [see Eqs. (IV-11) and (IV-12)]. Using 10 mb as an upper limit for the elastic cross section, we find that the maximum value of x_k is 0.66.

We have listed in Table VI the branching ratios from Alvarez et al. and ours. There are large discrepancies between the $\bar{K}N$ and the $\Lambda\pi$ ratios. The disagreement between the $\bar{K}N$ ratios is considerable--we find that if the spin is 3/2, there is only one chance in 600,000 that x_k is smaller than 0.04, which is the upper limit set in the Alvarez et al. experiment for x_k. If the spin is 5/2 we find that there is only one chance in 60,000 that x_k is smaller than 0.04. We realize that we have tacitly assumed that the spin can be only 3/2 or 5/2 but, as we shall see, angular distributions certainly do not favor spin values greater than 5/2. These discrepancies require an explanation.

The branching ratio indicates how strongly a given channel is coupled to the resonance. In Fig. 31 we have drawn two diagrams showing what happens as far as $Y_1^*(1660)$ production and decay are concerned, in our experiment and in the Alvarez et al. experiment. If $Y_1^*(1660)$ were a narrow resonance and traveled very far before decaying we would expect identical branching ratios in both experiments. But this is not the case, because the resonance is 40 MeV wide. This corresponds to a mean decay length of only 1.0 fermi, and final-state interactions can therefore take place. Furthermore, in the Alvarez et al. experiment, reactions such as

$$K^- + p \rightarrow K^*(885) + N;\ K^*(885) \rightarrow \bar{K} + \pi \qquad \text{(IV-19)}$$

and

$$K^- + p \rightarrow Y^*(1660) + \pi;\ Y^*(1660) \rightarrow \bar{K} + N, \qquad \text{(IV-20)}$$

can take place simultaneously. These two final states overlap considerably, and interferences can take place between these two production processes. The same is true, in the Alvarez et al. experiment, of

Table VI. Branching ratios for $Y_1^*(1660)$[a]

	Experiment I[b]	Experiment II[c]
$\Lambda\pi$	0.31	< 0.09
$\Sigma\pi$	0.27	0.22 ± 0.06
$\Lambda\pi\pi$	0.18	0.16 ± 0.05
$\Sigma\pi\pi$	0.18	0.25 ± 0.06
$\bar{K}N$	< 0.04	> 0.16[d]

a. The branching ratios for the two experiments have been normalized so that their sums are equal to 1.0.

b. The experiment of Alvarez et al.

c. This experiment.

d. We have used in this column the spin 3/2 lower limit for x_k (see discussion). We remind the reader that in our experiment $x_k > 0.09$ for spin 5/2.

the two reactions

$$K^- + p \rightarrow Y_1^*(1660) + \pi; \quad Y_1^*(1660) \rightarrow \Lambda + \pi \qquad \text{(IV-21)}$$

and

$$K^- + p \rightarrow Y_1^*(1385) + \pi; \quad Y_1^*(1385) \rightarrow \Lambda + \pi . \qquad \text{(IV-22)}$$

In our data, no such interferences or final-state interactions can take place. We therefore conclude that the discrepancies must be attributed to interferences and final-state interactions.

It appears that the quantum numbers of a resonance should be determined, whenever possible, in reactions in which the resonance is "formed," as in Fig. 31a, rather than in reactions in which it is "produced," as in Fig. 31b. Production reactions are very useful for finding resonant states, since they cover wide ranges of recoil energy. But because of final-state interactions and interferences, which can be very large [as we have seen in the case of the $Y_1^*(1660)$], no reliable information can be extracted on the spin, parity, and branching ratios in production experiments. However, once a resonance has been found in production reactions, one can set up another experiment and analyze it in a formation reaction.

2. Angular Distributions and the Spin of $Y_1^*(1660)$

Forgetting for a while the existence of the resonance, let us examine the angular distributions by themselves for what information we can obtain directly on the amplitudes present in the region.

The plots of the probability P in Figs. 8 through 10 indicate that at 620 MeV/c and 760 MeV/c only $\cos^2\theta$ terms are needed to fit the angular distributions. At 850 MeV/c, on the other hand, $\cos^3\theta$ terms are clearly required. In Appendix B a complete expansion of the differential cross section in terms of the amplitudes up to $f_{5/2}$ has been given [Eq. (A-8)]. It is clear from that formula that if an angular distribution contains terms up to $\cos^2\theta$ the only large amplitudes that can contribute are $s_{1/2}$, $p_{1/2}$, and either $p_{3/2}$ or $d_{3/2}$. Large amounts of other amplitudes would immediately lead at least to large $\cos^3\theta$ terms through interferences.

All the 620 MeV/c angular distributions are quite similar to those obtained at 510 MeV/c by Ferro-Luzzi et al.[8] These authors found that the s-wave amplitude dominated the K^--p system at 510 MeV/c, and it seems reasonable to assume that this is also the case at 620 MeV/c. At 760 MeV/c the coefficients of $\cos^2\theta$ are much larger than at 620 MeV/c in all the distributions, and this indicates that p waves have now come in strongly. At 850 MeV/c, the $\cos^3\theta$ terms indicate that d waves are also present.

Let us examine now what can be said about the spin of $Y_1^*(1660)$ on the basis of the angular distributions. It is very hard to make quantitative estimates of the likelihood of a given spin, because we lack a knowledge of the angular distributions at closely spaced points around the resonance region. This knowledge is very important if we are to clearly determine what the background amplitudes are in the region. Indeed, with several points in the resonance region one can assume, as a first approximation, that all the variations in the coefficients of the angular distributions are due to the resonant amplitude and, from this, background amplitudes can be determined. Furthermore, with many points, an overall fit to the data is possible, and confidence levels can be given.

In our case a fit is not possible, and the confidence we have in the various spin assignments cannot be expressed quantitatively. However, to distinguish between the spin values we remember that no significant $\cos^3\theta$ terms are required in any of the angular distributions at 760 MeV/c. This means, as we have said, that $s_{1/2}$, $p_{1/2}$ and either $p_{3/2}$ and $d_{3/2}$ are present at that momentum. This already points to spin 3/2 for $Y_1^*(1660)$. However, a question remains: would it be easy for a resonant amplitude of angular momentum 5/2 or greater, with the partial widths that we have given in Table VI, to have passed unnoticed in the angular distributions? This is the question we examine now.

As can be seen in Appendix B, the $\cos^3\theta$ terms contain such products as 15 Re $s^*_{1/2}\, f_{5/2}$ and its parity transform 15 Re $p^*_{1/2}\, d_{5/2}$. The $\cos^3\theta$ terms are therefore very sensitive to 5/2 amplitudes. We

want to find out the lower limit that we can set on $s_{1/2}$ in order to obtain an observable interference with an $f_{5/2}$ resonant amplitude, considering the errors in our $\cos^3\theta$ terms at 760 MeV/c. Taking $\Sigma^-\pi^+$, and assuming that a $\cos^3\theta$ term of 0.08 (see Fig. 19) could have been distinguished, we find that an $s_{1/2}$ amplitude of 0.05 corresponds to such a situation if $s_{1/2}$ and $f_{5/2}$ are in phase. The cross section for such an $s_{1/2}$ amplitude would be given by $4\pi\lambda^2 |0.05|^2$; namely, only 0.06 mb. If the $s_{1/2}$ and $f_{5/2}$ are at 45° with respect to each other, the $s_{1/2}$ becomes 0.085, and the corresponding cross section is 0.12 mb. One of course obtains identical results for the parity transforms of these two amplitudes (i.e., $p_{1/2}$ and $d_{5/2}$). In the other channels, similarly small nonresonant amplitudes would give detectable $\cos^3\theta$ terms. Now, looking at Figs. 26 and 27, we see that the background cross sections are clearly much larger than the resonant cross sections, both in the elastic and in the inelastic channels. A large part of this nonresonant background is evidently due to $s_{1/2}$ and $p_{1/2}$ amplitudes. It therefore appears that spin 3/2 is more consistent with our data than a higher value of the spin because in the latter case we expect large $\cos^3 2$ terms. However, we do not consider this analysis as a proof that the resonance is spin 3/2. Only another experiment with at least 6 to 8 data points in the resonance region will provide a final answer to the spin question.

V. CONCLUSION

We have shown that the $K^- + p$ system is mainly s wave at 620 MeV/c, and s and p wave at 760 MeV/c, and that d waves have further appeared at 850 MeV/c. We have shown that $Y_1^*(1660)$ is produced at 760 MeV/c, and its branching ratios have been determined. The size of the inelastic cross section at 760 MeV/c rules out spin 1/2 for $Y_1^*(1660)$. Finally, the absence of $\cos^3\theta$ terms in the angular distributions indicates that spin values greater than 3/2 are not consistent with our data.

We have not discussed the parity of $Y_1^*(1660)$. Only a knowledge of the energy dependence of the $\sin\theta \cos\theta$ terms in the polarizations of the $\Lambda\pi^0$ and $\Sigma\pi$ channels can settle this question. It is interesting to note that Glashow and Rosenfeld have recently shown that the $Y_1^*(1660)$ fits very well in the "eightfold way" classification of the resonant states if it is a $d_{3/2}$ resonance.[24]

ACKNOWLEDGMENTS

I wish to thank Professor Luis W. Alvarez for his support and encouragement, and I am very grateful to Dr. Joseph J. Murray and Professor Arthur H. Rosenfeld for their invaluable guidance throughout this work. It is also a pleasure to thank Professor Donald H. Miller and Professor Robert D. Tripp for stimulating discussions on the problems of resonance theory, and Dr. Massimiliano Ferro-Luzzi for his contributions in the data analysis. I also wish to thank Dr. Orin I. Dahl and J. Peter Berge for their help in the programming problems, and Dr. Janos Kirz for many helpful suggestions. Finally, many thanks are due to Mr. Cornell Dudley for coordinating the scanning and measuring part of the experiment.

This work was done under the auspices of the U. S. Atomic Energy Commission.

APPENDICES

A. Clebsch-Gordan Coefficients

We list here for reference the Clebsch-Gordan coefficients for the two-body reactions. Symbol T denotes an amplitude of given total angular momentum and parity, and the subscript refers to I spin:

$$T(K^- p) = 1/2\,(T_0(\bar{K}N) + T_1(\bar{K}N)), \tag{A-1}$$

$$T(\bar{K}^0 n) = 1/2\,(T_0(\bar{K}N) - T_1(\bar{K}N)), \tag{A-2}$$

$$T(\Sigma^+\pi^-) = 1/\sqrt{2}\,(1/\sqrt{3}\,T_0(\Sigma\pi) - 1/\sqrt{2}\,T_1(\Sigma\pi)), \tag{A-3}$$

$$T(\Sigma^-\pi^+) = 1/\sqrt{2}\,(1/\sqrt{3}\,T_0(\Sigma\pi) + 1/\sqrt{2}\,T_1(\Sigma\pi)), \tag{A-4}$$

$$T(\Sigma^0\pi^0) = 1/\sqrt{2}\,(1/\sqrt{3}\,T_0(\Sigma\pi)), \tag{A-5}$$

$$T(\Lambda\pi^0) = 1/\sqrt{2}\,(T_1(\Lambda\pi)). \tag{A-6}$$

It is clear that the sum of the squares of the amplitudes for the charged states of a given channel contains no interference terms, and is merely equal to one-half the sum of the squares of the pure I-spin amplitudes for that channel; for example,

$$|T(\Sigma^-\pi^+)|^2 + |T(\Sigma^+\pi^-)|^2 + |T(\Sigma^0\pi^0)|^2 = 1/2\{|T_0(\Sigma\pi)|^2 + |T_1(\Sigma\pi)|^2\}. \tag{A-7}$$

It can easily be shown that this last statement is also true for three-body final states.

B. Differential Cross Sections up to Angular Momentum 5/2

To represent the orbital angular momentum l and the total angular momentum J of an amplitude, we use a letter (from the standard spectroscopic notation) to denote l, and a subscript to that letter to denote 2J. The center-of-mass angle is denoted by θ. We have:[25]

$$k^2\sigma(\theta) = \{|s_1|^2 + |p_1|^2 + |p_3|^2 + |d_3|^2 + \frac{9}{4}(|d_5|^2 + |f_5|^2) + 2\,\mathrm{Re}[-(s_1^* d_3 + p_1^* p_3) - \frac{3}{2}(s_1^* d_5 + p_1^* f_5) + \frac{3}{2}(d_3^* d_5 + p_3^* f_5)]\}$$

(A-8) continued

REFERENCES

1. Ronald R. Ross, Elastic and Charge-Exchange Scattering of K^- Mesons in Hydrogen (Ph. D. Thesis), Lawrence Radiation Laboratory Report UCRL-9749, June 21, 1961 (unpublished).
2. Paul Nordin, Jr., S- and P-Wave Interactions of K^- Mesons in Hydrogen (Ph. D. Thesis), Lawrence Radiation Laboratory Report UCRL-9489, November 21, 1960 (unpublished).
3. W. Graziano and S. G. Wojcicki, $K^- + p$ Interactions at 1.15 BeV/c, Lawrence Radiation Laboratory Report UCRL-10177, May 29, 1962 (unpublished).
4. W. H. Barkas and A. H. Rosenfeld, Data for Elementary-Particle Physics, Lawrence Radiation Laboratory Report UCRL-8030 Rev. (April 1963 Edition) (unpublished).
5. G. Alexander, L. Jacobs, G. R. Kalbfleisch, D. H. Miller, G. A. Smith, and J. Schwartz, in Proceedings of the International Conference on High Energy Physics, CERN, 1962 (CERN Scientific Information Service, Geneva 23, Switzerland), p. 320.
6. L. W. Alvarez, M. H. Alston, M. Ferro-Luzzi, D. O. Huwe, G. R. Kalbfleisch, D. H. Miller, J. J. Murray, A. H. Rosenfeld, J. B. Shafer, F. T. Solmitz, and Stanley G. Wojicicki, Phys. Rev. Letters 10, 184 (1963).
7. P. Bastien and J. P. Berge, Phys. Rev. Letters 10, 188 (1963).
8. M. Ferro-Luzzi, R. D. Tripp, and M. B. Watson, Phys. Rev. Letters 8, 28 (1962). See also R. D. Tripp, M. B. Watson, and M. Ferro-Luzzi, Phys. Rev. Letters 8, 175 (1962); and Mason B. Watson, K^--Proton Interactions Near 400 MeV/c (Ph. D. Thesis), Lawrence Radiation Laboratory Report UCRL-10175, September 1962 (unpublished).
9. P. L. Bastien, O. I. Dahl, J. J. Murray, M. B. Watson, R. G. Ammar, and P. Schlein, in Proceedings of an International Conference on Instrumentation for High-Energy Physics (Interscience Publishers, Inc., New York, 1961), p. 299.
10. Joseph J. Murray, in Proceedings of an International Conference on Instrumentation for High-Energy Physics (Interscience Publishers, Inc., New York, 1961), p. 25.

11. J. Peter Berge, S- and P-Wave Analysis of $Y_1^*(1385)$ Production in $K^- + p \rightarrow \Lambda + \pi^+ + \pi^-$ at 760 and 850 MeV/c.

12. This microscope was built under the direction of Mr. Jack Franck, whence its name.

13. Arthur H. Rosenfeld, in Proceedings of the International Conference on High-Energy Accelerators and Instrumentation (CERN Scientific Information Service, Geneva, 1959), p. 533. Also see W. E. Humphrey, "A Description of PANG Program," Alvarez Group Memoranda Nos. 111 and 115, Lawrence Radiation Laboratory, Berkeley, California (unpublished).

14. Arthur H. Rosenfeld and James N. Snyder, Rev. Sci. Instr. 33, 181 (1962).

15. Dave Johnson, The EXAMIN System, Alvarez Group Memorandum No. 271, Dec. 1961 (unpublished).

16. L. Champomier, SUMX, Alvarez Group Memorandum No. 389, June 1962 (unpublished).

17. A. H. Rosenfeld, Nucl. Instr. Methods 20, 1 (1963).

18. Burton J. Moyer, Rev. Mod. Phys. 33, 367 (1961).

19. A. H. Rosenfeld, Reference Manual for KICK IBM Program, UCRL-9099, May 1961 (unpublished).

20. If we were to do this experiment again we would use histograms instead of ideograms. Before we give the reasons why ideograms were used let us explain the differences between histograms and ideograms. Ideograms appear to be useful in two respects: first to obtain resolution functions and secondly to establish the central value of a peak in a given distribution. On the other hand, a peak in an ideogram will be approximately $\sqrt{2}$ times as wide as the corresponding peak in a histogram. Furthermore ideograms make it difficult to evaluate the statistical significance of a peak in a distribution. It seems therefore that data should be plotted in the form of histograms although the corresponding ideogram forms a useful complement to them. In this particular experiment using histograms rather than ideograms would have yielded the same results. Now, at the beginning of this experiment, we did not take into account the fact that

in 0 prong + V events, the beam tracks appear shorter than they really are because of gaps at the end of the tracks. This, in turn, tends to make the missing mass recoiling against the (K^-, Λ) system appear larger than it really is. In particular, in the $\Lambda\pi^0$ final state, the mass of the π^0 was shifted upward; ideograms were useful to determine how this central value varied. After the cause of the trouble was found, we did not revert to histograms. Using histograms rather than ideograms in this experiment would not have changed the results significantly. We wish to thank Professor Rosenfeld for a useful discussion on this problem.

21. O. Chamberlain, K. M. Crowe, D. Keefe, L. T. Kerth, A. Lemonick, Tim Maung, and T. F. Zipf, Phys. Rev. 125, 1696 (1962).

22. R. H. Dalitz and S. F. Tuan, Ann. Phys. 10, 307 (1960).

23. Derek Prouse (University of California Los Angeles), private communication, 1962.

24. S. L. Glashow and A. M. Rosenfeld, Phys. Rev. Letters 10, 192 (1963).

25. Frank S. Crawford, Partial Waves through $F_{5/2}$, Alvarez Group memorandum No. 403 (unpublished).